J. Fluid Mech. (2003), *vol.* 476, *pp.* 357–388.
DOI: 10.1017/S0022112002002999 Printed in the United Kingdom

Elliptic and triangular instabilities in rotating cylinders

By CHRISTOPHE ELOY, PATRICE LE GAL AND STÉPHANE LE DIZÈS

Institut de Recherche sur les Phénomènes Hors Équilibre, CNRS UMR 6594, Universités Aix-Marseille I et II, 49, rue Joliot Curie – BP 146, 13384 Marseille Cedex 13, France

(Received 28 January 2002 and in revised form 4 September 2002)

In this article, the multipolar vortex instability of the flow in a finite cylinder is addressed. The experimental study uses a rotating elastic deformable tube filled with water which is elliptically or triangularly deformed by two or three rollers. The experimental control parameters are the cylinder aspect ratio and the Reynolds number based on the angular frequency.

For Reynolds numbers close to threshold, different instability modes are visualized using anisotropic particles, according to the value of the aspect ratio. These modes are compared with those predicted by an asymptotic stability theory in the limit of small deformations and large Reynolds numbers. A very good agreement is obtained which confirms the instability mechanism; for both elliptic and triangular configurations, the instability is due to the resonance of two normal modes (Kelvin modes) of the underlying rotating flow with the deformation field. At least four different elliptic instability modes, including combinations of Kelvin modes with azimuthal wavenumbers $m = 0$ and $m = 2$ and Kelvin modes $m = 1$ and $m = 3$ are visualized. Two different triangular instability modes which are a combination of Kelvin modes $m = -1$ and $m = 2$ and a combination of Kelvin modes $m = 0$ and $m = 3$ are also evidenced.

The nonlinear dynamics of a particular elliptic instability mode, which corresponds to the combination of two stationary Kelvin modes $m = -1$ and $m = 1$, is examined in more detail using particle image velocimetry (PIV). The dynamics of the phase and amplitude of the instability mode is shown to be predicted well by the weakly nonlinear analysis for moderate Reynolds numbers. For larger Reynolds number, a secondary instability is observed. Below a Reynolds number threshold, the amplitude of this instability mode saturates and its frequency is shown to agree with the predictions of Kerswell (1999). Above this threshold, a more complex dynamic develops which is only sustained during a finite time. Eventually, the two-dimensional stationary elliptic flow is reestablished and the destabilization process starts again.

1. Introduction

Strong vorticity filaments have been evidenced in turbulent flows experimentally (Cadot, Douady & Couder 1995) and numerically (see Jiménez & Wray 1998 and references therein). The discovery of these coherent structures has renewed the interest in vortex dynamics, as it was outlined by Pullin & Saffman (1998) in their recent review. The formation of these filaments was related to shear flow instabilities by Passot *et al.* (1995). However, several issues concerning the dynamics of these structures in

turbulent flows and their breakdown are still open. In recent numerical simulations of transition to turbulence of gravity waves, Arendt, Fritts & Andreassen (1998) showed the presence of Kelvin modes on vortex filaments which cannot be explained by the usual vorticity tilting and stretching arguments. One aim in this study is to provide a possible mechanism for the apparition of these modes in terms of an instability of vorticity filaments caused by the surrounding turbulent flow: namely the *multipolar instability*.

A model commonly used for vorticity filaments in turbulence is the Burgers (1948) vortex. This axisymmetric vortex, of Gaussian vorticity profile, is a stationary solution of the Navier–Stokes equations for which viscous diffusion is exactly compensated by axial stretching. Moffatt, Kida & Ohkitani (1994) (see also Ting & Tung 1965) showed that an external strain field would induce a first-order correction to the Burgers model which deforms the streamlines inside the core from circles to ellipses. Using numerical simulations of turbulent flows (Kida & Ohkitani 1992), Moffatt *et al.* (1994) also showed that the energy dissipation field of vortex filaments is reproduced remarkably well by this elliptically distorted Burgers vortex. Prochazka & Pullin (1998) later showed the bi-dimensional stability of Moffatt *et al.*'s (1994) solution but Eloy & Le Dizès (1999) established its sensitivity to the tri-dimensional *elliptic instability*. This instability could explain the appearance of Kelvin modes on the filament since they are its natural modes.

The elliptic instability was (re)discovered by Pierrehumbert (1986) and Bayly (1986) in the context of parallel shear flows as a secondary instability of Kelvin–Helmoltz vortices (see also Bayly, Holm & Lifschitz 1996 and references therein). However, the first stability studies of vortices with elliptic streamlines are due to Gledzer *et al.* (1975), Moore & Saffman (1975) and Tsai & Widnall (1976). In a recent review, Kerswell (2002) stressed how the elliptic instability has been discovered in the 1970s and then rediscovered in 1986 in a different context (see this review for a comprehensive bibliography on the subject). The physical mechanism of this instability can be understood as follows. First, we should assume the existence of Kelvin modes which are neutral normal modes characterized by their axial wavenumber, azimuthal wavenumber and frequency $[k, m, \omega]$. Then, the elliptic deformation of the streamlines should be interpreted as an intrinsic mode of characteristics $[k, m, \omega] = [0, \pm 2, 0]$. The instability mechanism is a triadic resonance of this intrinsic mode and two Kelvin modes of the same axial wavenumber, same frequency and azimuthal wavenumbers differing by 2. Moore & Saffman (1975) showed that combinations of stationary ($\omega = 0$) and helical ($m = \pm 1$) Kelvin modes are always resonant and unstable. However, as pointed out by Billant, Brancher & Chomaz (1999), the elliptic instability is not limited to these particular combinations. Indeed, Eloy & Le Dizès (2001) analysed all the possible resonances for the Rankine vortex and demonstrated that a combination of a bulging Kelvin mode ($m = 0$) and a splitting mode ($m = 2$) could appear spontaneously.

The mechanism of the elliptic instability has been generalized to flows with higher azimuthal symmetry by Le Dizès & Eloy (1999) and Eloy & Le Dizès (2001). It appears that a vortex subject to an n-fold multipolar strain field is always unstable if $n = 2$, 3 or 4, giving rise to what has been called the *multipolar instability*. For symmetry of higher degree, the flow is unstable only if the external strain field is sufficiently strong.

The experimental study of the elliptic instability began with the pioneering work of Gledzer *et al.* (1974, 1975). They used a rigid cylinder of elliptic cross-section (an ellipsoid in their 1974 paper) filled with water seeded with reflective particles. This

container was rotated until solid-body rotation was reached and then it was sharply stopped. During the transient decay of the flow, the streamlines are elliptical and this may lead to the elliptic instability. Later Chernous'ko (1978) used the same set-up and studied the wavelength of the instability as a function of two control parameters of the experiment: the eccentricity of the elliptic cylinder and its aspect ratio. His results agree remarkably well with the theoretical prediction of Gledzer & Ponomarev (1992) for undulating modes (a combination of two stationary helical Kelvin modes). Nevertheless, this set-up has two main inconveniences: first, the instability develops on a transiently decaying flow (thus during a limited time); and a competitive centrifugal instability appears near the wall. To avoid the shortcomings of Gledzer's experiment, Malkus (1989) and Malkus & Waleffe (1991) used a deformable elastic cylinder rotated at constant angular speed. Using a belt or two rollers, this cylinder could be deformed elliptically, such that the axes of the ellipse were kept still in the laboratory frame. This experiment produced a stationary elliptic basic flow on which the undulating modes already reported by Gledzer *et al.* (1975) were observed. This experiment showed the intermittent character of the instability at high rotation rate. Indeed, the amplitude of the instability modes was not observed to saturate in the regimes studied; a cycle of instability growth, mode breakdown and relaminarization took place, as will be described in detail.

Besides the physics of small-scale turbulent structures, another important field where the elliptical instability could have a considerable interest is astro- and geophysics. Indeed, the tidal effects experienced by rotating planets or other astrophysical objects created by the proximity of others are of great interest. In particular, we can easily imagine that the Earth molten iron outer core is deformed by the gravitational strains of the Moon and Sun and therefore is subject to an elliptical instability. Kerswell (1994) estimated that the global loss due to friction and ohmic dissipation has the same order of magnitude as the growth rates of unstable modes in rotating spheroids. Thus, the energy gained by the elliptic instability could very well be part (with convective and precessional instabilities) of the energy source required to sustain the geodynamo effect. For instance, Kerswell & Malkus (1998) interpreted Io's magnetic signature by the distortion of its inner molten core due to the gravitational field of Jupiter. The first experiments on rotating flows inside ellipsoids were due to Gledzer *et al.* (1974). Later, a series of experiments and calculations by Aldridge *et al.* (1997) and Seyed-Mahmoud, Henderson & Aldridge (2000) also showed the existence of such an instability inside a rotating deformable shell which models the Earth's interior with its inner solid core. Note that, in this particular geometry, the mathematical existence of inertial waves deserves its own particular mathematical analysis (Rieutord & Valdetarro 1997).

In addition, the elliptic instability was observed in open flow configurations such as counter-rotating (Leweke & Williamson 1998*a*) and co-rotating vortex filaments (Meunier & Leweke 2001, 2002). It was also identified as a mechanism for secondary instability in parallel shear flows (Bayly, Orszag & Herbert 1988) and wakes (Leweke & Williamson 1998*b*).

In the present study, we investigate the elliptic instability and its generalization to the 'triangular' instability both experimentally and theoretically. Our work can be viewed as a continuation and a generalization of earlier studies by Malkus and co-workers (Malkus 1989; Malkus & Waleffe 1991). It is also a more detailed account of the results briefly reported in Eloy, Le Gal & Le Dizès (2000). The paper is organized as follows. In § 2, the set-up and the experimental procedure are presented. In § 3, the theoretical linear stability of this flow is addressed using asymptotic analysis in

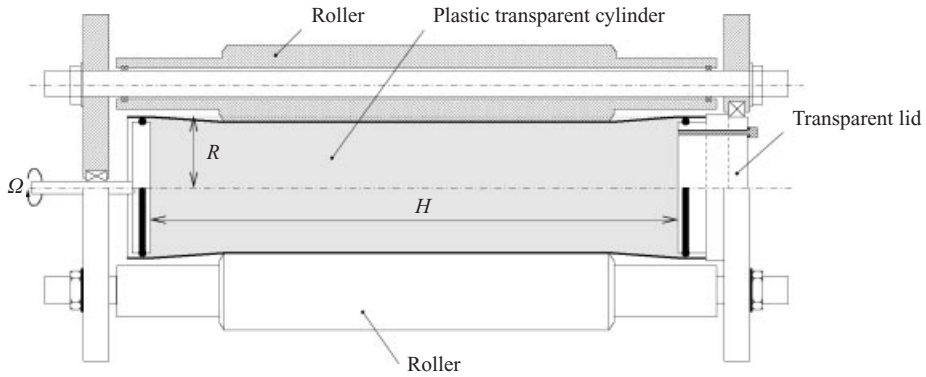

FIGURE 1. Experimental set-up. A plastic deformable cylinder, filled with water is rotated at constant angular speed Ω. Two or three rollers can be positioned to apply a dipolar or tripolar constraint on the cylinder.

the large-Reynolds-number and weak-deformation limits. This allows us to take into account viscosity and finite cylinder aspect ratio which are shown to select particular modes in § 3.2. The experimental results obtained by visualization and particle image velocimetry (PIV) measurements are presented in § 4 for low- and high-Reynolds-number flows. Theoretical and experimental instability diagrams are compared in § 4.1 for both elliptic and triangular configurations. Sections 4.2 and 4.3 focus on the weakly nonlinear regime and the intermittent cycle of the stationary mode of the elliptic instability. Finally, the results are summarized in § 5.

2. Experimental set-up

The experimental set-up used in this study (figure 1) has been inspired by the work of Malkus (1989) (see also Malkus & Waleffe 1991). The core of the experiment is a transparent plastic extruded cylinder of radius $R = 2.75\,\mathrm{cm}$ and variable length $H = 8$–$23\,\mathrm{cm}$. Thanks to the small thickness of its elastic wall (0.5 mm), this cylinder can be deformed in the stationary laboratory frame with two or three rollers parallel to its axis. This deformed cylinder is rotated at chosen angular speed ($\Omega = 0.5$–$10\,\mathrm{rad\,s^{-1}}$) by a 300 W electric motor. The angular speed, measured by an optical coder linked to the axis, is shown to be reasonably stable (variations are kept within 2%).

The cylinder, set with its axis parallel to the vertical direction (in contrast to all the pictures presented in this paper which have been rotated by 90° for convenience), is filled with water by an aperture located at an endwall. For visualizations, anisotropic particles (Kalliroscope) are added to the water and a light sheet is formed in a plane containing the cylinder axis, using a 4 W argon laser. This visualization technique does not allow us to have precise information on the velocity field as shown by Gauthier, Gondret & Rabaud (1998). Nevertheless, the axial wavelength and the frequency of the mode appearing in the cylinder can be measured by filming the flow with a standard video camera and analysing the images.

Particle image velocimetry (PIV) has also been performed by adding calibrated 30 μm reflective spherical particles to the water. A laser sheet perpendicular to the axis is used to illuminate the particles. A 1000×1000 pixel DCC video camera is placed at one end of the cylinder and the particles are filmed through the transparent lid (see figure 1). The video camera is controlled by a computer which can record 300 images, thus allowing us to compute 150 velocity fields for each experiment. The numerical algorithm used to process the images has been developed using the Matlab

software by Meunier & Leweke (2001, 2002) and can therefore be run on a common PC computer. Typically, it takes about 4 h to compute 150 velocity fields (containing 60×60 velocity vectors each).

To limit experimental artefacts, attention is paid to several crucial points. First, the orthogonality of the endwalls and the cylinder axis is checked with good precision to avoid precession type instability. The mechanical properties of the elastic cylinder being modified by its ageing, care is also taken by using cylinders for fairly short periods of time and by avoiding important constraints. Finally, the presence of bubbles in the flow is prevented by waterproofing the whole cylinder.

The two dimensionless control parameters of this experiment are:

$$Re = \frac{\Omega R^2}{\nu} \text{ : Reynolds number,} \tag{2.1a}$$

$$\frac{H}{R} \text{ : aspect ratio,} \tag{2.1b}$$

which can be varied in the limits $Re = 300$–8000 and $H/R = 3$–8.2. From a practical point of view, two sets of rollers have been used allowing the aspect ratio to be varied in the ranges $H/R = 3$–4 and 7–8.2. The third control parameter of the experiment would be the strength of the constraint imposed by the rollers on the cylinder, but the variation of this parameter has not been considered in the present study.

In all the experiments presented in this paper, the same protocol has been followed:

(i) The two or three rollers used to deformed the cylinder are positioned;

(ii) When the fluid is assured to be at rest (after at least 10 min), the cylinder is suddenly rotated at constant angular speed;

(iii) During all the experiment, the roller position and the cylinder speed are kept constant.

The linear stability of the flow produced by this set-up is addressed theoretically in the next section. Experimental results are presented in § 4 and discussed in § 5.

3. Linear stability study

3.1. *Inviscid analysis*

The experimental arrangement described above is aimed at producing a flow of constant vorticity subjected to a dipolar or tripolar strain. The basic flow can therefore be described, in cylindrical coordinates (r, θ, z), by the streamfunction:

$$\psi = -\tfrac{1}{2}r^2 + \frac{\varepsilon}{n} r^n \sin(n\theta), \tag{3.1}$$

where ε measures the deformation of the streamlines (ε is the eccentricity of the ellipses for $n = 2$) and n is the degree of azimuthal symmetry of the flow or equivalently the number of rollers deforming the elastic cylinder (see figure 2). Here, the variables are made dimensionless using the characteristic length R and time Ω^{-1}. The position of the rollers in the experiment is such that the deformation of the streamlines is $\varepsilon \approx 0.10$ for $n = 2$ and $\varepsilon \approx 0.12$ for $n = 3$. In the present theoretical analysis, ε is considered as a small parameter. The outer streamline of the flow, given by $\psi = -\frac{1}{2}$, corresponds to the cylinder boundary. Note that the streamfunction (3.1) describes a flow with largest velocities in the large curvature regions whereas, in the experiment, velocity is uniform on the boundary. This difference can be taken into account by considering viscous boundary layers on the wall. However, as will be shown below, these boundary layers have negligible influence on the selection of the instability modes in the limit of small ε.

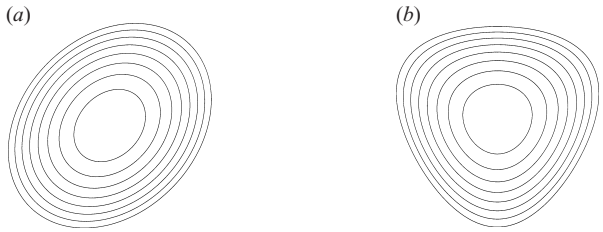

FIGURE 2. Streamlines of the basic flow given by (3.1). The parameters are $\varepsilon = 0.25$ and: (*a*) $n = 2$; (*b*) $n = 3$. The flow is rotating counterclockwise.

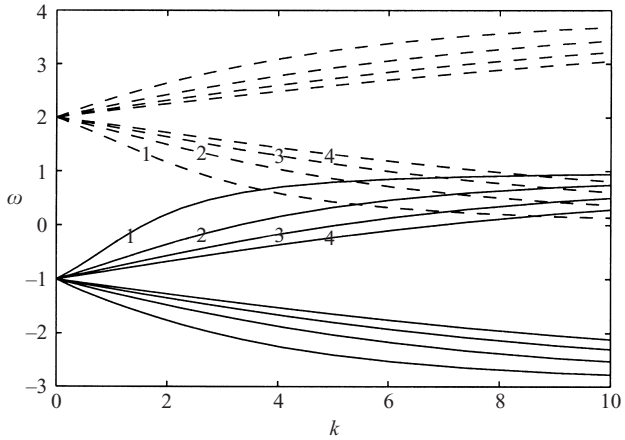

FIGURE 3. Dispersion relation of the Kelvin modes inside a cylinder. Eight branches are shown in the (k, ω)-plane for $m = -1$ (solid lines) and $m = 2$ (dashed lines).

The stability of the basic flow (3.1) has been studied using a local approach by Le Dizès & Eloy (1999). It has been shown to be unstable in the limit of vanishing viscosity with the dimensionless growth rate $\sigma = \frac{9}{16}\varepsilon$ for $n = 2$ and $\sigma = \frac{49}{32}\varepsilon$ for $n = 3$. The stability of the same flow embedded in an irrotational flow was considered by global methods in Eloy & Le Dizès (2001). The selection of the instability modes by both finite size and viscous effects was analysed in details. Here, the basic flow (3.1) is embedded in a cylinder which makes the stability results slightly different. However, since the method of analysis is the same as in Eloy & Le Dizès (2001), we shall not detail the calculation but only outline its different stages in the following.

For purely axisymmetric flow ($\varepsilon = 0$), normal Kelvin modes (Kelvin 1880) can be superimposed linearly to the basic flow. Their velocity field can be written as:

$$\boldsymbol{v}(r, \theta, z, t) = \boldsymbol{U}(r)\, \mathrm{e}^{\mathrm{i}(kz + m\theta - \omega t)} + \text{c.c.}, \tag{3.2}$$

where k, m and ω are the axial wavenumber, the azimuthal wavenumber and the frequency and $\boldsymbol{U}(r)$ is given in the Appendix (the notation c.c. simply refers to the complex conjugate). These Kelvin modes are marginally stable for an axisymmetric and inviscid flow. Upon imposing the boundary condition on the cylinder wall (in $r = 1$), a dispersion relation connecting the different wavenumbers can be found (see the Appendix). This dispersion relation is illustrated in figure 3. For a chosen azimuthal wavenumber m, there is an infinity of branches in the (k, ω)-plane which accumulate in $\omega = m$ in the limit of small k and in $\omega = m \pm 2$ in the limit of infinite k.

	Elliptic			Triangular		
i	$(-1,1,i)$	$(0,2,i)$	$(1,3,i)$	$(-1,2,i)$	$(0,3,i)$	$(1,4,i)$
1	1.58	2.33	3.04	3.67	5.18	6.61
2	3.29	4.12	4.92	7.18	8.81	10.36
3	5.06	5.92	6.75	10.72	12.40	14.01

TABLE 1. Table of the axial wavenumbers k for a few principal modes. These wavenumbers can be slightly modified in a cylinder of finite aspect ratio and in the presence of viscosity.

In the limit of small deformation ε, Kelvin modes still exist. As mentioned in the introduction, two Kelvin modes can resonate with the basic flow if they have same k, same ω and have azimuthal wavenumbers m_1 and m_2 such that $m_2 - m_1 = n$. For instance, in figure 3, the crossing points of the dispersion relations for $m_1 = -1$ and $m_2 = 2$ then correspond to points of resonance for a triangular deformation of the vortex ($n = 3$). A stability study similar to that of Eloy & Le Dizès (2001) shows that all Kelvin mode resonances are unstable. However, crossing points of branches with the same label (see figure 3) are significantly more amplified than the others. These particular combinations of Kelvin modes are called *principal modes* and are denoted

$$(m_1, m_2, i), \tag{3.3}$$

hereinafter, where m_1 and m_2 are the azimuthal wavenumbers of the two Kelvin modes and i is the common label of the dispersion relation branches. Note that i is an increasing function of the axial wavenumber k. Table 1 gives the value of the first axial wavenumbers k as a function of i for a few principal modes. Owing to the asymptotic symmetry of the dispersion relation, the frequency of principal modes satisfies $\omega \approx \frac{1}{2}(m_1 + m_2)$. In the following, only the principal modes will be taken into account in the analysis since their inviscid growth rate is about 100 times larger than that of other combinations of resonant Kelvin modes.

For an infinite cylinder and in the limit of vanishing viscosity, the growth rate of the different principal modes can be found by similar techniques to those detailed in Eloy & Le Dizès (2001). The results for the inviscid growth rate σ_{i} are summarized in figure 4. For elliptic deformation ($n = 2$), the maximum inviscid growth rate is $\sigma_{\mathrm{i}} = \frac{9}{16}\varepsilon$. It is reached in the limit of large k either when the azimuthal wavenumber m_1 tends to infinity for a fixed label i or when i tends to infinity for fixed m_1. However, the instability is not very selective in the elliptic case, since the inviscid growth rates of the different principal modes are all within 10% of the maximum. For the triangular deformation ($n = 3$), the inviscid growth rate is maximum in the limit of large azimuthal wavenumber m_1, for fixed label i. This maximum is $\sigma_{\mathrm{i}} = \frac{49}{32}\varepsilon$. Note that, in the triangular case, the selection of the different principal modes is much more efficient. As for the Rankine vortex (Eloy & Le Dizès 2001), the local maximum growth rate found in Le Dizès & Eloy (1999) is recovered in the limit of large k for elliptic deformation and in the limit of large m_1 and k for triangular deformation.

3.2. *Effects of viscosity and aspect ratio*

As seen above, in the absence of viscosity and for infinite cylinder, the maximum growth rate is reached for infinite k. Under these approximations, the selected modes would have infinite axial wavenumber for $n = 2$ and infinite axial and azimuthal wavenumber for $n = 3$. Of course, this result cannot hold when viscosity is added

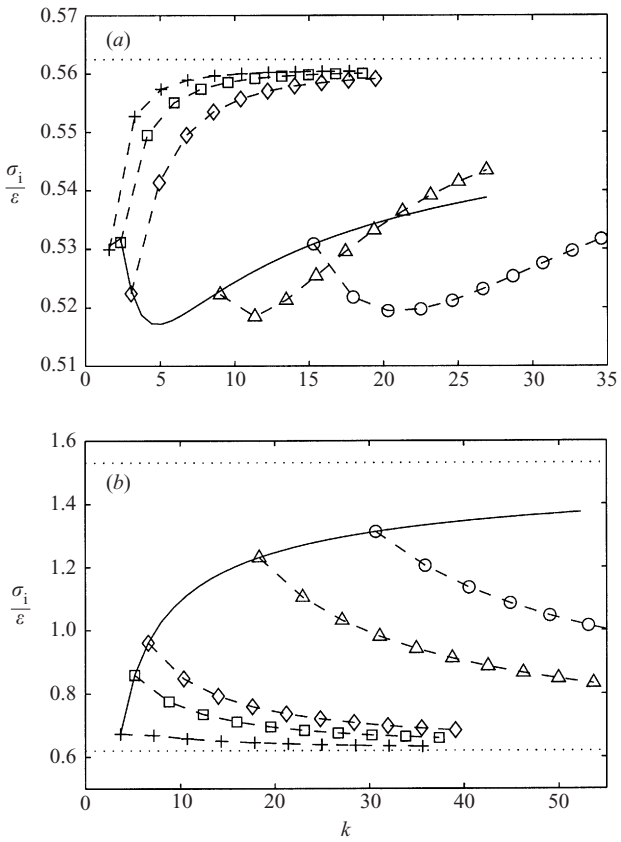

FIGURE 4. Inviscid growth rate σ_i for (a) $n = 2$ and (b) $n = 3$ as a function of the axial wavenumber k. The growth rate of principal modes $(m_1, m_1 + n, i)$ are presented with: +, $m_1 = -1$; □, $m_1 = 0$; ◇, $m_1 = 1$; △, $m_1 = 10$ and ○, $m_1 = 20$. The solid line corresponds to the first principal modes $(m_1, m_1 + n, 1)$ for $-1 \leqslant m_1 \leqslant 39$. The asymptotic values of the inviscid growth rate are pictured by dotted lines: (a) $\sigma_i = \frac{9}{16}\varepsilon$; ($b$) $\sigma_i = \frac{49}{8\pi^2}\varepsilon$ and $\sigma_i = \frac{49}{32}\varepsilon$.

since it tends to damp the modes with the largest wavenumbers. In this section, boundary viscous effects and volume viscous effects are first taken into account in the stability analysis. Then, the effect of the finite aspect ratio of the cylinder will be analysed. As will be shown, these two effects can efficiently select particular modes. A similar study, in a different context, has also been carried out by Racz & Scott (2001*a*).

As described above, the inviscid (dimensionless) growth rate of principal modes is $\sigma_i = O(\varepsilon)$. The distinguished scaling for viscosity is obtained when the decay rate due to viscous effects is of same order. Now the effects of *volume* viscous damping account for a decay rate $\sigma_{vol} = -O(Re^{-1}k^2)$. In addition, Kelvin modes, as described by (3.2), do not satisfy viscous boundary conditions on the wall of the cylinder. To achieve this condition, we have to consider a viscous boundary layer on the wall. This layer has a thickness $\delta = O(Re^{-1/2})$. Because of the z- and θ-dependence of Kelvin modes, this boundary layer is not uniform, giving rise to pumping flow in the core of the cylinder. Therefore, it modifies the principal mode at an $O(Re^{-1/2})$ order. It results in a *surface* viscous effect of decay rate $\sigma_{surf} = -O(Re^{-1/2})$ (see Greenspan 1968 for details). The distinguished scaling is then obtained when $Re = O(\varepsilon^{-2})$. For this scaling, volume viscous effects are negligible as soon as $k \ll Re^{1/4}$ and therefore

should not be taken into account in the analysis for $k = O(1)$. Note, however, that the damping rate of viscous surface effects depends slightly on the geometry of the mode whereas volume viscous effects have the property of selecting modes with the smallest wavenumbers (since their damping rate is proportional to k^2). Besides, when volume and surface viscous effects are calculated for $\varepsilon \approx 0.1$ (as is the case in the experiments presented in this paper), they are shown to be of same order as soon as $k \approx 1$. For these reasons, we have retained volume viscous effects in the analysis.

The different effects can be summarized by writing down the amplitude equations. The two Kelvin modes of azimuthal wavenumbers m_1 and m_2 have complex amplitudes $A_1(t)$ and $A_2(t)$, respectively, which follow the dynamical equations:

$$\frac{\mathrm{d}A_1}{\mathrm{d}t} = \varepsilon n_1 A_2 + (-Re^{-1/2}s_1 - Re^{-1}v_1 + \mathrm{i}(k-k_0)q_1)A_1, \tag{3.4a}$$

$$\frac{\mathrm{d}A_2}{\mathrm{d}t} = \varepsilon n_2 A_1 + (-Re^{-1/2}s_2 - Re^{-1}v_2 + \mathrm{i}(k-k_0)q_2)A_2, \tag{3.4b}$$

where the terms n_1 and n_2 are real numbers and describe the Kelvin mode interaction driven by the multipolar strain of strength ε. The terms s_1 and s_2 are complex numbers and correspond to the surface viscous effects whereas v_1 and v_2 are real and describe volume viscous effects. Finally, the last terms q_1 and q_2 are real and correspond to a shift in axial wavenumber k away from the perfectly resonant wavenumber k_0 (calculated in the absence of viscosity). In the absence of viscosity and for $k = k_0$, we recover the inviscid growth rate $\sigma_{\mathrm{i}}^2 = \varepsilon^2 n_1 n_2$. All the constants appearing in these equations are $O(1)$ and have been computed from the formulae given in the Appendix for each principal mode (m_1, m_2, i).

Viscous effects can be summarized by plotting the marginal stability curves (figure 5) of all principal modes in the (k, Re)-plane. Figure 5 shows that below a critical value of the Reynolds number ($Re_c = 435$ for $n = 2$, $\varepsilon = 0.1$ and $Re_c = 398$ for $n = 3$, $\varepsilon = 0.12$), all modes are damped by viscosity and the flow is stable. Above this critical value a first mode is destabilized for a given axial wavenumber k. Both for $n = 2$ and 3, this mode corresponds to the mode with the smallest axial wavenumber. When the Reynolds number is increased again, a large number of modes gradually become unstable. Each principal mode is unstable over a finite band of axial wavenumbers. The width of these instability bands is roughly proportional to ε for large Re. Note that there is a non-trivial effect of viscosity which tends to modify slightly the resonant axial wavenumber and frequency of the principal modes as Re varies (this is due to the non-zero imaginary part of s_1 and s_2 in (3.4a, b)).

The selection of particular instability modes can also be performed by imposing a finite aspect ratio of the cylinder. Indeed, when the condition of no outward flow is imposed in $z = 0$ and $z = H/R$, some principal modes can be discarded. This condition is fulfilled only if the principal mode is a standing wave (formed as the superposition of two counter travelling waves) of axial wavenumber $k = l\pi R/H$, where l is an integer. For finite cylinder, the surface damping rate is also modified by additional bottom and top boundary layers. As in Kudlick (1966) (see also Racz & Scott 2001a), these viscous terms can be estimated by supposing that the boundary of the cylinder is sufficiently regular, i.e. the radius of curvature of the surface is always larger than the boundary-layer thickness. Even if this approximation does not hold near the edges of the cylinder, it gives a very good estimation of this viscous decay rate, as shown numerically by Kerswell & Barenghi (1995). Note that an alternative approach which avoids the problem associated with corners can also be used (see Racz & Scott 2001a).

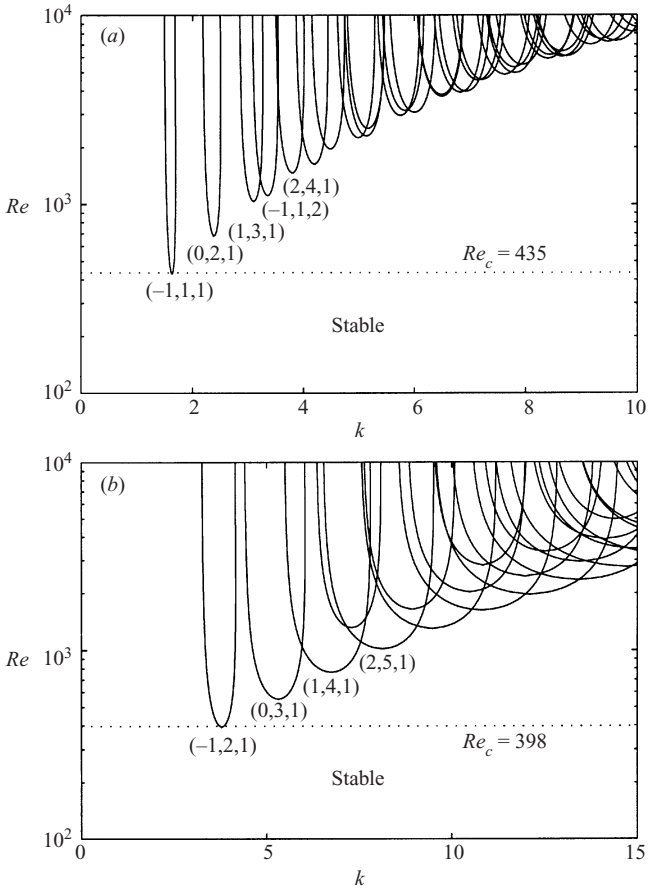

FIGURE 5. Marginal stability curves of all principal modes. These curves have been calculated for a infinite cylinder and: (*a*) $n = 2$, $\varepsilon = 0.10$; (*b*) $n = 3$, $\varepsilon = 0.12$.

The combined effects of viscous damping and mode selection by aspect ratio are summarized in figure 9. As a function of the two experimental control parameters (the Reynolds number and the aspect ratio), the principal mode with the largest growth rate is represented. This figure shows that, depending on the choice of the parameters, a large number of different principal modes should be observed. The mode selection is different in the elliptic and triangular cases. Indeed, for elliptic deformation, many modes can be selected over the available range of aspect ratios without varying the Reynolds number, whereas, for triangular deformation, the mode predicted at low Reynolds number is always the mode $(-1, 2, 1)$ as soon as $H/R > 5.6$. This difference is mainly because the mode wavenumbers k are larger in the triangular case (see table 1 and figure 5). To improve mode selection for $n = 3$, we would have to reduce the width of the instability bands by decreasing ε.

4. Experimental results

In this section, we present the results of the experimental study. First, the mode selection by the Reynolds number and the aspect ratio is analysed with flow visualizations and compared with the theoretical predictions. Then, the weakly nonlinear

regime of a particular mode (the stationary undulating mode of the elliptic instability) is studied using PIV measurements. Results in agreement with the amplitude equations are obtained. In § 4.3, the flow for large Reynolds number (far from the instability threshold) is described. In this regime, a cycle of instability growth and breakdown is evidenced and characterized.

4.1. *Low-Reynolds-number flow*

For Reynolds number slightly above the threshold, the observed flow evolution can be decomposed in three successive phases:

(i) The spin-up of the flow takes over on a time scale of order $\tau = H(Re/\Omega)^{1/2}$ as described by Wedemeyer (1964) and Watkins & Hussey (1977) for an axisymmetric cylinder.

(ii) Once solid-body rotation is achieved, a principal mode eventually grows after a time related to its growth rate (which varies typically between one minute and one hour).

(iii) The principal mode reaches a saturated amplitude. The flow is now time-periodic and z-periodic. Wavelength and frequency of the observed mode can be measured by image analysis.

To test the mode selection by varying the aspect ratio, four experiments have been carried out for an elliptic deformation at the same Reynolds numbers, for four different aspect ratios ($H/R = 7.13$, 7.49, 7.96 and 8.20). Figure 6 shows the flow obtained by Kalliroscope visualizations when the mode amplitude has reached saturation. In each case, the aspect ratio has been chosen such that an experimental wavenumber which is given by $k = l\pi R/H$, where l is an integer, is close to the most unstable theoretical wavenumber of a given mode. Here, for the four different aspect ratios, we should observe the modes $(1, 3, 1)$, $(-1, 1, 2)$, $(-1, 1, 1)$ and $(0, 2, 1)$, respectively (as seen in figure 9). The most unstable wavenumbers, which are calculated for an infinite Reynolds number and an infinite cylinder are reported in table 2 together with their frequency. The experimental wavenumber can be measured by counting the number of wavelengths observed along the cylinder (in figure 6 for instance, 3.5, 4, 2 and 3 wavelengths can be identified for each aspect ratio, respectively). These measured wavenumbers k_{exp} are not exactly equal to the theoretical most unstable wavenumbers. These slight differences in wavenumber as well as the finiteness of the Reynolds number can be taken into account in the theory. They induce a small shift in the frequencies $\Delta\omega$ which is indicated in table 2. The experimental frequency is obtained by image analysis of Kalliroscope visualizations. A spatio-temporal diagram is constructed by extracting the same horizontal line in each image of the video sequence and by laying the lines on the same figure (figure 7 for instance). These spatio-temporal diagrams show the time-periodicity of the flow and permit us to measure the frequencies ω_{exp} which are reported in table 2. Note that the modes displayed in figures 6(b) and 6(c) are stationary, as predicted by the theory. The two periodic modes shown in figures 6(a) and 6(d) also have frequencies very close to the theoretical predictions. These good agreements permit us to identify unambiguously the modes observed with the modes predicted by the theory.

The same experiments have been performed for the triangular deformation. Figure 8 shows visualizations of the modes $(-1, 2, 1)$ and $(0, 3, 1)$ and their associated spatio-temporal diagrams. Wavelength and frequency of these modes (measured with the same techniques as for elliptic deformation) are given in table 2. However, the frequency of the mode $(-1, 2, 1)$ at $Re = 1200$, measured in figure 8(c), is $\omega = 0.55$. This value is different from the theoretical prediction which is $\omega = 0.656$. This

n	mode	ω_{th}	ω_{exp}	$\Delta\omega$	k_{th}	k_{exp}	Figure
2	$(1,3,1)$	2.044	2.0	2.0×10^{-4}	3.035	3.1	6(a)
2	$(-1,1,2)$	0.000	0.00	0	3.286	3.4	6(b)
2	$(-1,1,1)$	0.000	0.00	0	1.579	1.6	6(c)
2	$(0,2,1)$	1.038	1.0	7.7×10^{-4}	2.326	2.3	6(d)
3	$(-1,2,1)$	0.656	0.55	8.8×10^{-4}	3.674	3.7	8(a)
3	$(0,3,1)$	1.608	1.5	3.4×10^{-3}	5.185	5.0	8(b)

TABLE 2. Theoretical prediction for the frequency ω_{th} and axial wavenumber k_{th} of a few principal modes (for inviscid flow and infinite cylinder) compared to experimental measurements ω_{exp} and k_{exp}. For $Re = 2500$ and for a cylinder of the same length as in the corresponding experiment, the theory predicts a slight shift of frequency $\Delta\omega$. The last column gives the number of the figure where the mode is displayed.

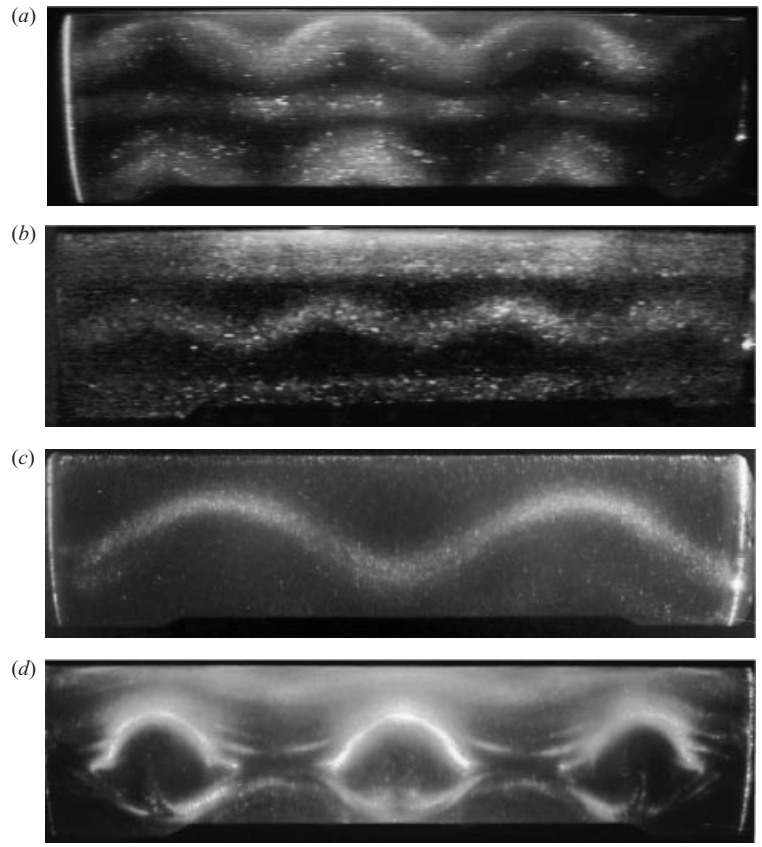

FIGURE 6. Elliptic instability. Visualizations of the flow for $n = 2$, $Re = 2500$ and: (a) $H/R = 7.13$; (b) 7.49; (c) 7.96; (d) 8.20. They correspond to the principal modes $(1,3,1)$, $(-1,1,2)$, $(-1,1,1)$ and $(0,2,1)$, respectively. Note that (c) and (d) are also reproduced in Kerswell (2002) (unfortunately, with inverted captions).

discrepancy may come from nonlinear effects which tend to detune the frequency when the mode amplitude grows, as shown by Waleffe (1989). For a Reynolds number closer to the threshold ($Re = 460$), the measured frequency is closer to the predicted one: $\omega = 0.65$ (not shown here). The difference between the frequencies of the modes $(-1,2,1)$ and $(0,3,1)$ is particularly visible on the spatio-temporal diagrams of figures

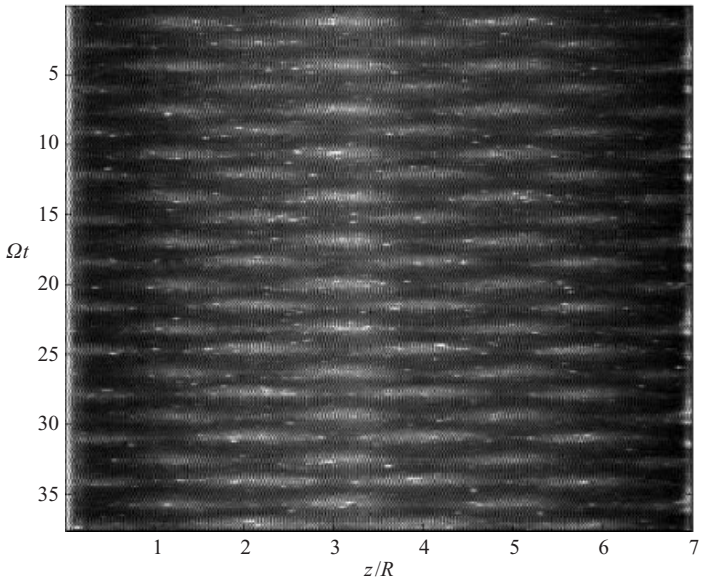

FIGURE 7. The spatio-temporal diagram of the mode $(1, 3, 1)$. Experimental parameters are $n = 2$, $Re = 2500$ and $H/R = 7.13$. The signal is here time-periodic with a frequency $\omega_{exp} = 2\Omega$ where Ω is the angular frequency of the cylinder rotation.

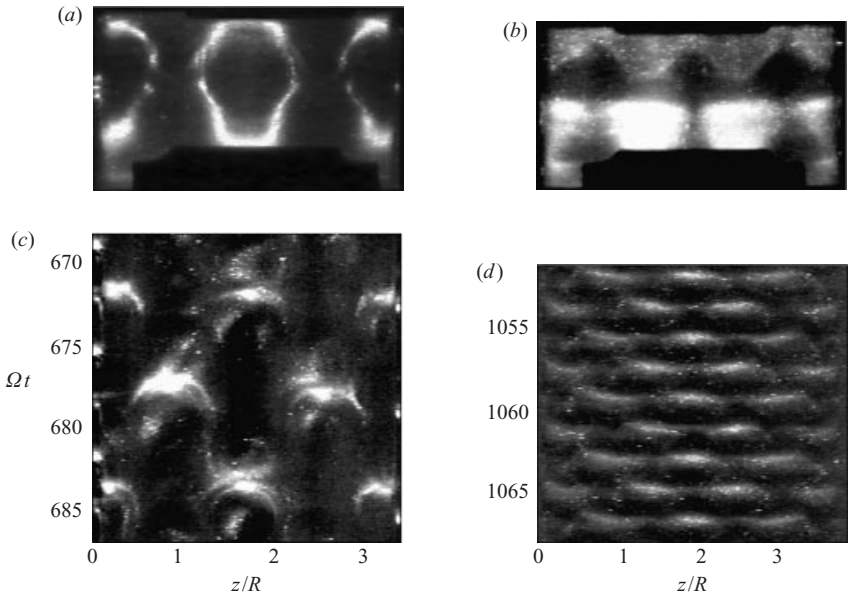

FIGURE 8. Triangular instability. Visualizations of the modes (a) $(-1, 2, 1)$ and (b) $(0, 3, 1)$. Experimental parameters are: $n = 3$, $Re = 1200$ and (a) $H/R = 3.4$, (b) 3.8. The spatio-temporal diagrams (c) and (d) correspond to visualizations (a) and (b), respectively.

8(c) and 8(d) where the time axes have the same scale. Several radial structures have been observed in the Kalliroscope visualization. However, as already mentioned, it is hazardous to associate them with any radial structure of the velocity field (see Gauthier *et al.* 1998).

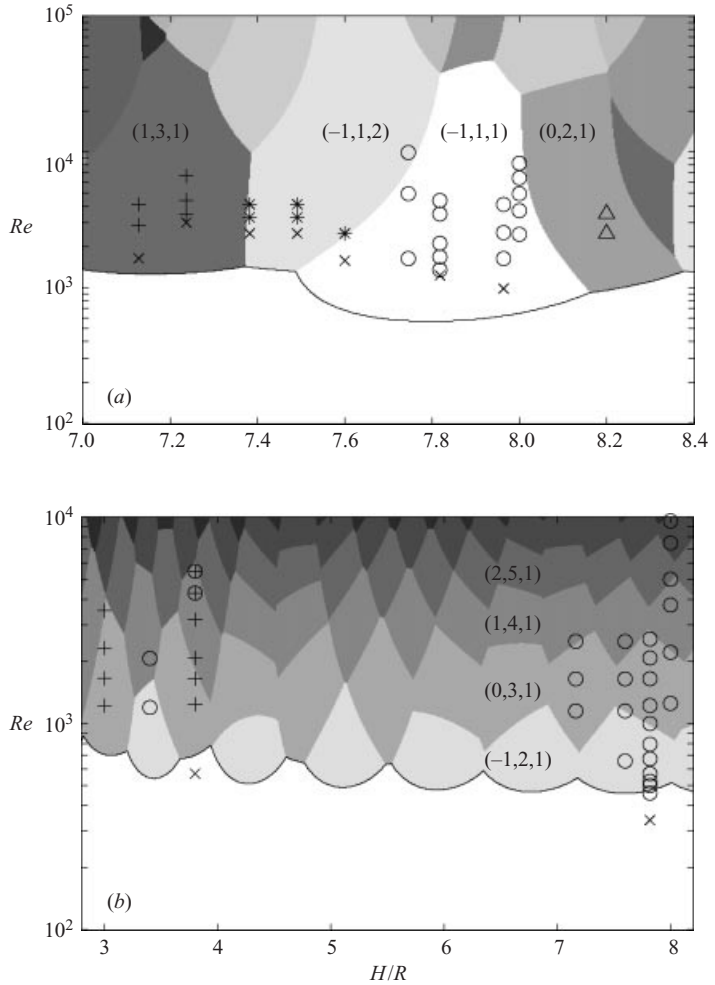

FIGURE 9. Comparison of the predicted and observed principal mode as a function of the experimental control parameters $(H/R, Re)$ for (a) $n = 2$ and (b) $n = 3$. Each grey tone corresponds to the most dangerous principal mode, i.e. the mode with the largest growth rate. The symbols represent experiments: (a) ○, $(-1, 1, 1)$; ∗, $(-1, 1, 2)$; △, $(0, 2, 1)$; +, $(1, 3, 1)$ and (b) ○, $(-1, 2, 1)$; +, $(0, 3, 1)$. ×, visualizations where no distinct mode was observed.

The comparison between theoretical predictions and experimental observations is summarized in figure 9. For each experiment (a single symbol in figure 9), the observed principal mode is reported and compared to the most unstable mode found theoretically. In the elliptic case, the agreement is excellent except close to the threshold where no distinct principal mode has been observed. This is probably due to the small amplitude of the mode for low Reynolds numbers in agreement with the supercriticality of the bifurcation (Mason & Kerswell 1999). It will be seen in § 4.2, that PIV permits us to observe the mode $(-1, 1, 1)$ closer to the threshold.

In the triangular case (figure 9*b*), there is good agreement between the observed and predicted principal modes close to the threshold. However, when the Reynolds number is increased, the mode predicted by linear stability theory is not recovered experimentally. Indeed, we always observe the same mode as the Reynolds number is increased. This phenomenon could be related to either nonlinear or transient effects.

Unusual effects have also been found for $H/R = 3.8$, $Re = 4300$ and 5500. For these parameters, a non-periodic cycle between the principal modes $(-1, 2, 1)$ and $(0, 3, 1)$ has been observed reproducibly.

4.2. *The stationary undulating mode* $(-1, 1, 1)$

In this section, we focus on the stationary mode $(-1, 1, 1)$ which was previously observed in a similar experiment by Malkus (1989) and by Malkus & Waleffe (1991). This particular mode can be observed for an elliptic deformation of the cylinder ($n = 2$), for an aspect ratio ranging from $H/R = 7.7$ to 8 and for a large range of Reynolds numbers (as described by figure 9). All the results presented in the following were obtained for an aspect ratio of $H/R = 7.96$ which corresponds to the visualization of two wavelengths of the mode $(-1, 1, 1)$ along the length of the cylinder. We first present the characteristics of the flow produced by the mode $(-1, 1, 1)$, then the theoretical results obtained by a weakly nonlinear analysis. Finally, the experimental results obtained by PIV measurements are compared to the theory.

By definition, the principal mode $(-1, 1, 1)$ is the sum of two counter helical stationary modes which give rise to a stationary wave. If we neglect the elliptic deformation of the streamlines, the total velocity field can be written, in the linear regime, as

$$\boldsymbol{v}(r, \theta, z) = \begin{pmatrix} 0 \\ r \\ 0 \end{pmatrix} + 2a \begin{pmatrix} U_r(r)\cos(kz)\sin(\theta - \varphi) \\ U_\theta(r)\cos(kz)\cos(\theta - \varphi) \\ U_z(r)\sin(kz)\sin(\theta - \varphi) \end{pmatrix}, \tag{4.1}$$

where the first term corresponds to the solid-body rotation and the second term is the stationary wave of complex amplitude $A = a\mathrm{e}^{-\mathrm{i}\varphi}$, where a and φ are two real numbers. The functions $U_r(r)$, $U_\theta(r)$ and $U_z(r)$ are given in the Appendix. To satisfy the inviscid boundary conditions, the radial velocity is such that $U_r(1) = 0$ and the axial wavelength k such that $kH/R = 4\pi$, i.e. $k = 1.579$ as shown in the previous section. There are particular points within the cylinder where the velocity field is exactly zero. The coordinates (r, θ, z) of these points are such that $\sin(\theta - \varphi) = 0$ and r satisfies the following implicit equation

$$2aU_\theta(r)\cos(kz)\cos(\theta - \varphi) + r = 0, \tag{4.2}$$

where z can take any value. The projection of the velocity field in a plane perpendicular to the z-axis is always a rotation around a particular point whose position in the plane $\theta = \varphi$ is given by (4.2).

The position of this new rotation axis is obtained by solving (4.2) for all z. In the linear stability theory, the angle φ is predicted to remain zero: this corresponds to an undulation of the vortex centre in the plane of stretching ($\theta = 0$). Figure 10 compares a Kalliroscope visualization of the mode $(-1, 1, 1)$ and the loci of the centre of rotation for an amplitude $a = 0.03$. Note that we have taken into account, in figure 10(b), the optical effect of the convex cylinder surface which makes the mode appear about $\frac{1}{3}$ larger. In figure 10(a), we can see that the demarcation line between the dark zone and the illuminated zone corresponds remarkably well with the position of the rotation centre in figure 10(b). For this particular mode, the Kalliroscope technique would allow us to obtain quantitative information on the flow field, which is not generally the case. Theoretically, if the rotation centre stays in the plane of visualization, we should be able to measure the mode amplitude a as a function of time by this method. However, this is not possible in practice as nonlinear effects tend to rotate the plane of undulation and therefore to shift the rotation centre

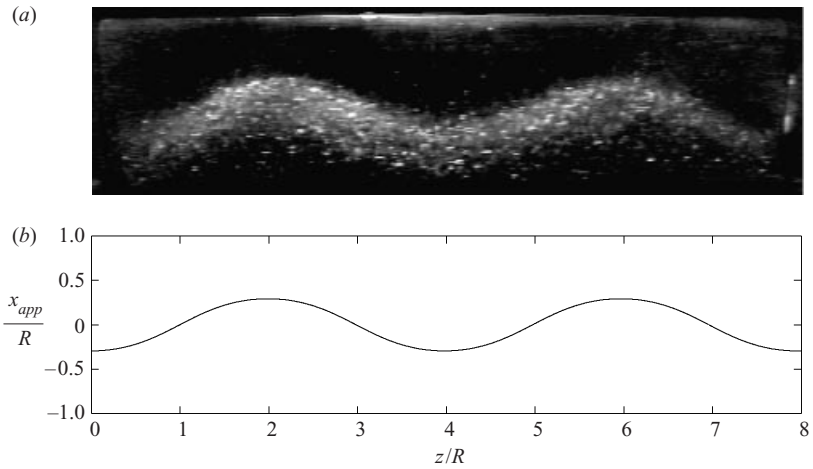

FIGURE 10. Comparison between visualization and theoretical prediction of the mode $(-1, 1, 1)$. (a) Kalliroscope visualization for $Re = 2500$ and $H/R = 7.96$ in the (x, z)-plane (i.e. $\theta = 0$) and (b) theoretical prediction of the centre of rotation by the linear stability theory for a mode amplitude $A = 0.03$.

outside the plane of visualization. For this reason, we analyse experimentally the flow in a plane perpendicular to the cylinder axis and use PIV measurements to track the evolution of the rotation centre.

From a theoretical point of view, to understand the dynamics of the mode amplitude and particularly the rotation of its phase φ, we have to consider the nonlinear modification of the basic flow. Waleffe (1989) first performed a weakly nonlinear analysis of the elliptic instability in the absence of viscosity (see also Sipp 2000) and Racz & Scott (2001*b*) carried out a viscous weakly nonlinear analysis of a parametric instability similar to the elliptic instability. Racz & Scott (2001*b*) showed that the effects of viscosity are not as simple as initially guessed by Waleffe (1989). Finally, Mason & Kerswell (1999) performed a weakly nonlinear analysis of the elliptic instability (in a cylinder with modified boundary conditions) focusing on the saturated state of the mode amplitude. Here, in order to compare theory with the PIV measurements, we have to perform a weakly nonlinear analysis of the elliptic instability including viscous effects and dynamical effects. Since the analysis is quite long and does not involve new methods, the reader is referred to the above papers for technical details. In the present paper, we merely outline the analysis for the distinguished scaling and we then jump to the amplitude equations.

Following classical asymptotic methods, the amplitude A is expanded in powers of the small eccentricity ε. The distinguished scaling for weakly nonlinear effects is obtained when the amplitude is $O(\varepsilon^{1/2})$. The Reynolds number is chosen to be $O(\varepsilon^{-2})$ such that the viscous flow induced by boundary layers is $O(\varepsilon^{3/2})$ (this viscous flow is proportional to $Re^{-1/2}A$). The nonlinear correction of the basic flow forced by the principal mode is a $O(\varepsilon)$ geostrophic flow. This flow has vanishing axial and radial velocity and its azimuthal velocity $\boldsymbol{v}_0$ depends only on radius r. It can be decomposed on the basis of Bessel functions $J_1(K^{(i)}r)$ all vanishing in $r = 1$:

$$\boldsymbol{v}_0(r) = \sum_{i=1}^{\infty} a_0^{(i)} J_1(K^{(i)}r), \tag{4.3}$$

with each real amplitude $a_0^{(i)}$ of order ε.

The amplitude A of the mode $(-1,1,1)$ and the amplitudes $a_0^{(i)}$ are supposed to vary on a slow time scale εt such that $\mathrm{d}A/\mathrm{d}t = O(\varepsilon^{3/2})$ and $\mathrm{d}a_0^{(i)}/\mathrm{d}t = O(\varepsilon^2)$. The amplitude equations for A and $a_0^{(i)}$ are therefore obtained by solvability conditions at orders $\varepsilon^{3/2}$ and ε^2, respectively. At order $\varepsilon^{3/2}$, the dynamics of A is driven by the interaction of the mode $(-1,1,1)$ with the geostrophic mode giving rise to a flow proportional to $a_0^{(i)}A$ and by the triple interaction of the mode $(-1,1,1)$ with itself producing a flow proportional to $|A|^2A$. The equations describing the dynamics of the geostrophic flow are obtained at order ε^2. They result from the nonlinear interaction of the mode $(-1,1,1)$ with the elliptic deformation and the boundary-layer corrections. Finally, both the mode $(-1,1,1)$ and the geostrophic flow are damped by viscosity. The balance of this $O(Re^{-1/2})$ damping term with the $O(\varepsilon)$ instability growth rate justifies *a posteriori* the scaling chosen for Re.

The resulting amplitude equations are (still with $A = a\mathrm{e}^{-\mathrm{i}\varphi}$):

$$\frac{\mathrm{d}a}{\mathrm{d}t} = (\varepsilon\sigma_\mathrm{i}\cos 2\varphi - Re^{-1/2}\mu_0)a, \tag{4.4a}$$

$$\frac{\mathrm{d}\varphi}{\mathrm{d}t} = \delta + Da^2 - \varepsilon\sigma_\mathrm{i}\sin 2\varphi + \sum_{i=1}^{\infty}\xi^{(i)}a_0^{(i)}, \tag{4.4b}$$

$$\frac{\mathrm{d}a_0^{(i)}}{\mathrm{d}t} = 2\varepsilon\lambda_1^{(i)}a^2\cos 2\varphi + Re^{-1/2}\lambda_2^{(i)}a^2 - Re^{-1/2}\mu_1^{(i)}a_0^{(i)}, \tag{4.4c}$$

with the inviscid growth rate $\sigma_\mathrm{i} = 0.5312$ and the nonlinear coefficient $D = 2.015$. The damping coefficients are $\mu_0 = 0.801 + 9.97Re^{-1/2}$, $\mu_1^{(i)} = 0.125 + K^{(i)^2}Re^{-1/2}$ where the first term of μ_0 and $\mu_1^{(i)}$ originates from viscous boundary layers and the second term from volumic viscous effects. The constants $K^{(i)}$ appearing in $\mu_1^{(i)}$ and the other coefficients $\lambda_1^{(i)}$, $\lambda_2^{(i)}$ and $\xi^{(i)}$ are given in table 3 (for $i \leqslant 4$). Here, as above, we have included the viscous volumic effects in the viscous coefficients μ_0 and μ_1 even if they appear at a larger order. The first amplitude equation (4.4*a*) reflects the modification of the growth rate when the angle φ is not zero. It appears that the growth rate in the weakly nonlinear regime is simply equal to the linear growth rate multiplied by the factor $\cos 2\varphi$, which is the local normalized stretching rate for $\theta = \varphi$. In this equation, the viscous damping rate $Re^{-1/2}\mu_0$ also appears. The critical Reynolds number is obtained when growth and damping rates compensate, i.e. $\mu_0 Re^{-1/2} = \varepsilon\sigma_\mathrm{i}$ which gives $Re_c = 537$ (we recover the same critical Reynolds number as in the linear theory for $H/R = 8$). In (4.4*b*), the term δ reflects the detuning associated with aspect ratio variation which tends to modify the angle φ. In the following, the coefficient δ is assumed to be negligible, i.e. the cylinder is assumed to be perfectly tuned. In (4.4*b*), we can also see that the geostrophic flow modifies the angle φ. The third equation (4.4*c*) describes the dynamics of the geostrophic flow through the different amplitudes $a_0^{(i)}$. It is worth noticing that the coefficients $\lambda_1^{(i)}$, $\lambda_2^{(i)}$ and $\xi^{(i)}$ rapidly decay as i increases. This permits us to justify a truncation of the sum appearing in (4.4*b*). It is also important to note that $\lambda_1^{(i)}$ and $\lambda_2^{(i)}$ are of opposite sign. This means that elliptic and viscous effects tend to compensate when considering the evolution of the geostrophic flow.

As demonstrated by Racz & Scott (2001*b*) on a similar system, the equation system (4.4*a*)–(4.4*c*) admits non-trivial fixed points. The first equation gives the angle of those fixed points which simply satisfies $\cos 2\varphi = Re^{-1/2}\mu_0/\varepsilon\sigma_\mathrm{i}$. For this angle, elliptic destabilizing effects are exactly balanced by viscous damping. Note

i	$K^{(i)}$	$\xi^{(i)}$	$\lambda_1^{(i)}$	$\lambda_2^{(i)}$
1	3.83	−0.223	−18.47	43.50
2	7.01	−0.153	−3.33	9.36
3	10.2	0.056	0.76	−2.64
4	13.3	−0.033	−0.33	1.45

TABLE 3. The different coefficients appearing in the nonlinear amplitude equations (4.4*a*)–(4.4*c*) for $i \leqslant 4$. These coefficients are only valid for the mode $(-1, 1, 1)$ and for $H/R = 8$.

that the amplitude a of the fixed point does not intervene in the fixed point angle. Figures 11 and 12 illustrate the possible dynamical behaviours of amplitude A for different Reynolds numbers. To obtain these figures, the equation system (4.4*a*)–(4.4*c*) has been solved numerically with the initial conditions $a = 10^{-5}$, $\varphi = 0$ and $a_0^{(i)} = 0$ for all i. When the amplitude is small, the dynamics follow the property of linear stability analysis, i.e. the amplitude a grows exponentially and φ remains zero. As a continues to grow, the first effect of nonlinearity is to shift the angle φ, thus decreasing the growth rate, as described by (4.4*a*). Eventually, the amplitude A converges towards a fixed point by spiralling in the complex plane (as seen in figure 12). The oscillating behaviour is more and more pronounced as the Reynolds number increases. For infinite Reynolds number, the nonlinearity has a peculiar effect. Indeed, in this case, a should eventually decrease back to zero after a given time, as stressed by Sipp (2000). However, this kind of trajectory is singular; for any finite Reynolds number, the trajectory always converges to a fixed point different from zero.

To compare the theoretical predictions of the weakly nonlinear stability theory with experimental results, we have performed PIV measurements. For this purpose, the cylinder is illuminated by a laser sheet in the plane $z/H = 0.75$, corresponding to a maximum displacement of the rotation centre. The time interval between two images can be varied from 5 to 100 ms according to the rotation frequency of the cylinder. As illustrated by figure 13, the PIV algorithm allows us to measure the projection of the velocity field in the plane of the laser sheet. Thus, it provides the position of the rotation centre. Both φ and a can be determined from this position. The angle φ corresponds to the physical angle between the direction of stretching and the position of this rotation centre. The amplitude a can be inferred from equation (4.2) for $\cos(kz) = 1$, by measuring the distance r between the rotation centre and the centre of the cylinder.

A succession of PIV analyses permits us to follow the evolution of a and φ as a function of time. Such evolutions are shown in figure 14 for three different Reynolds numbers. For all Reynolds numbers, the first stage of the experiment is the spin-up of the flow (not shown in these figures). During spin-up, a large part of the core of the cylinder is motionless, thus not permitting us to define precisely the position of the rotation centre. After spin-up, the rotation centre is located near the cylinder centre, i.e. the mode amplitude a is small. At this stage, the measurement of the angle φ is impossible (on the left of the dashed line in figure 14*b*). Eventually, the mode amplitude grows until it reaches a saturated state ($a = 0.04$ for $Re = 790$ and $a = 0.06$ for $Re = 1600$) and as it grows, the angle φ increases from zero to a fixed value ($\varphi = 14^\circ$ for $Re = 790$ and $\varphi = 26^\circ$ for $Re = 1600$). For $Re = 1600$, saturation of amplitude occurs when $300 < \Omega t < 450$. For larger times, another dynamic begins

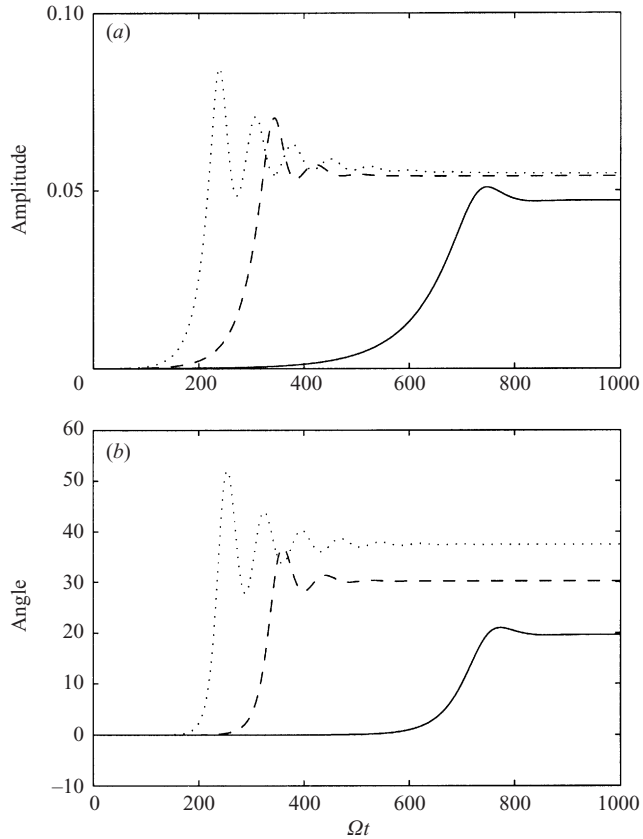

FIGURE 11. Illustration of the weakly nonlinear dynamics of the amplitude A by (a) its norm a and (b) phase ϕ for three different Reynolds numbers: ———, $Re = 790$; – – – –, 1600; · · · · · ·, 4700.

at time $\Omega t = 450$ which converges to a slightly different fixed point ($a = 0.07$ and $\varphi = 24°$). This new dynamic is reproducible and appears for $1000 < Re < 4000$. For the highest Reynolds number, $Re = 4700$, no saturation of the amplitude could be observed. This case is discussed in more detail in the next section.

For $Re = 790$, the agreement between theory and experiment is excellent (see figures 11 and 14), even if the amplitude a and angle φ of the fixed point observed in the experiment are slightly below the theoretical predictions. For $Re = 1600$, agreement is also quite good until $\Omega t = 450$. After this time, a new phenomenon, not taken into account in the weakly nonlinear theory (probably linked to a secondary instability as will be discussed below), comes into play and modifies the dynamics. Finally, for $Re = 4700$, the agreement is only correct during the exponential growth of the amplitude. After that, at time $\Omega t \approx 300$, the weakly nonlinear theory is not sufficient to describe the collapse of the amplitude.

Another way of comparing between weakly nonlinear theory and experiments is to plot the measured saturated amplitude a_{sat} and saturated angle φ_{sat} of the fixed points as a function of the Reynolds number, as in figure 15. In this figure, the value of the first fixed point reached by the amplitude is plotted (for $Re = 1600$, it corresponds to time $300 < \Omega t < 450$ as explained above) since we believe that the following dynamics are due to higher-order nonlinear effects not taken into account in the theory. In figure 14(a), the mode amplitude plotted is deduced from (4.2) for

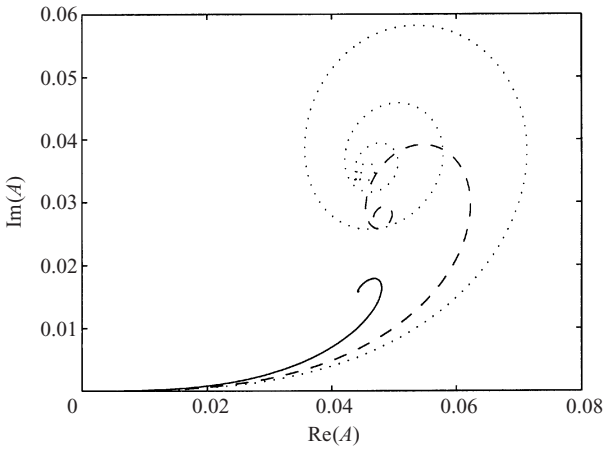

FIGURE 12. Trajectories of the amplitude A in the complex plane for the same Reynolds numbers as figure 11.

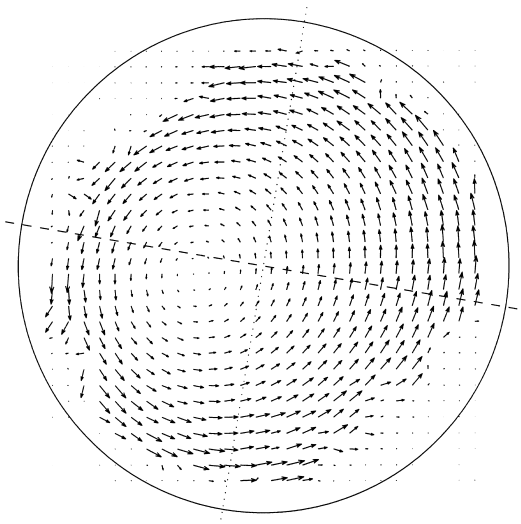

FIGURE 13. Illustration of a typical PIV velocity field of the mode $(-1, 1, 1)$. The dashed and dotted lines represent the stretching and compression axis, respectively. Close to the cylinder wall, the velocity field could not be measured because of illumination problems due to the presence of the rollers.

$\cos(kz)\cos(\theta - \varphi) = -1$. However, when a is large, an important geostrophic flow is produced which makes the amplitudes $a_0^{(i)}$ in the amplitude equation system (4.4) non-negligible. Knowing the angle φ and given the Reynolds number, the amplitudes $a_0^{(i)}$ of the geostrophic modes can be calculated at saturation using (4.4c). They are shown to be proportional to a^2. Thus, (4.2) can be modified into a second-order linear equation for a to take into account the geostrophic flow $\boldsymbol{v}_0(r)$. The solutions of this corrected equation correspond to the crosses in figure 15(a). This corrected saturated amplitude is about 20% lower than the amplitude shown in figure 14(a). It shows *a posteriori* that figure 14(a) gives only qualitative information on the mode dynamics.

From figure 15, we can see that there is a fairly good agreement between the predicted critical Reynolds number ($Re_c = 537$) and the one that could be inferred

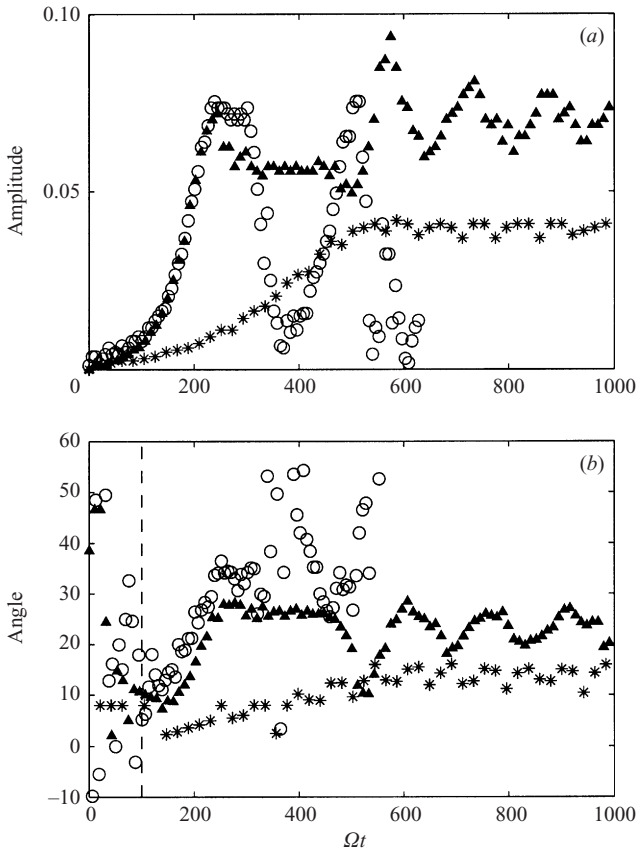

FIGURE 14. PIV measurements of (*a*) the amplitude and (*b*) the angle of the mode $(-1, 1, 1)$ as a function of time for *, $Re = 790$; △, 1600; ○, 4700.

from experiments. It is, however, important to mention that close to the threshold, the experiments were difficult to carry out owing to the fatigue of the cylinder material during the long period of time needed by the experiment (over 3 h). In figure 15(*b*), the measured saturated angle is compared with that predicted by (4.4*a*) for saturation. The good agreement confirms that the angle of saturation is simply the angle for which the stabilizing effect of viscosity and the destabilizing effect of ellipticity compensate. A small shift of 5° can be observed (it could be due to a lack of accuracy when defining the direction of stretching).

For $Re > 1000$, a periodic dynamic is observed superimposed on the stationary mode $(-1, 1, 1)$. This phenomenon can be associated with a secondary instability which has been identified in numerical simulations by Kerswell (1999) and Mason & Kerswell (1999) (see also Fabijonas, Holm & Lifschitz 1997; Lifschitz & Fabijonas 1996). By Kalliroscope visualization, we also observed the saturated state of this secondary instability as displayed in figure 16. As can be seen on these six successive images representing one period, a global oscillation of the flow is superimposed on the basic deformation of the axis of rotation due to the primary mode $(-1, 1, 1)$. During half a period of this secondary instability, the centre part of the flow is strongly illuminated in contrast to the end parts which stay darker. In the following half-period, the opposite situation occurs where the centre part of the flow stays

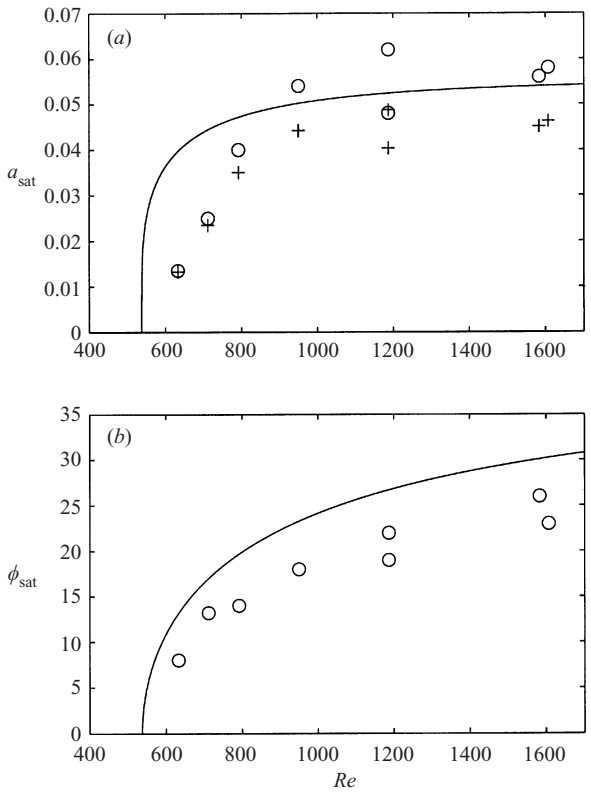

FIGURE 15. Bifurcation diagrams. (a) Saturated amplitude a_{sat} and (b) angle φ_{sat} as a function of the Reynolds number. The solid lines are deduced from weakly nonlinear theory; ○, PIV measurements; +, corrected amplitudes taking into account the geostrophic flow.

dark while the extremities of the cylinder are illuminated. However, owing to the difficulties in interpreting these Kalliroscope images (see Gauthier *et al.* 1998), we only calculate the frequency of these oscillations from the video images. The spatio-temporal diagram associated with this dynamic is shown in figure 17. In this figure, the periodicity of the flow is shown and its frequency is measured with good accuracy: $\omega = 2.31\Omega$. This is in agreement with the frequency of one of the instability modes predicted by Mason & Kerswell (1999): $\omega = 2.27\Omega$. Note that this frequency does not correspond to the frequency of the damped oscillations seen in figure 14(a) for $Re = 1600$ and $\Omega t > 450$ which are much slower: $\omega \approx 0.045\Omega$. Nevertheless, as for the fundamental mode, we expect the secondary instability to modify the basic flow by the generation of geostrophic modes through nonlinear interaction. This new geostrophic flow would imply a modification of the amplitude equations (4.4a)–(4.4c). The low-frequency damped oscillations of the mode amplitude seen in figure 14(a) are probably linked to the slow dynamics of the system of coupled modes. Apparently, for such low Reynolds numbers, the amplitude of the secondary instability mode also saturates and a final state composed of the saturated mode $(-1, 1, 1)$ and the saturated secondary instability mode can be obtained. As explained by Kerswell (1999), the physical mechanism of this secondary instability is a triadic resonance of the mode $(-1, 1, 1)$ with two Kelvin modes. For the frequency $\omega = 2.27\Omega$, these two modes are such that their axial, azimuthal wavenumbers and frequency are: $k_1 = \frac{1}{2}k_0$,

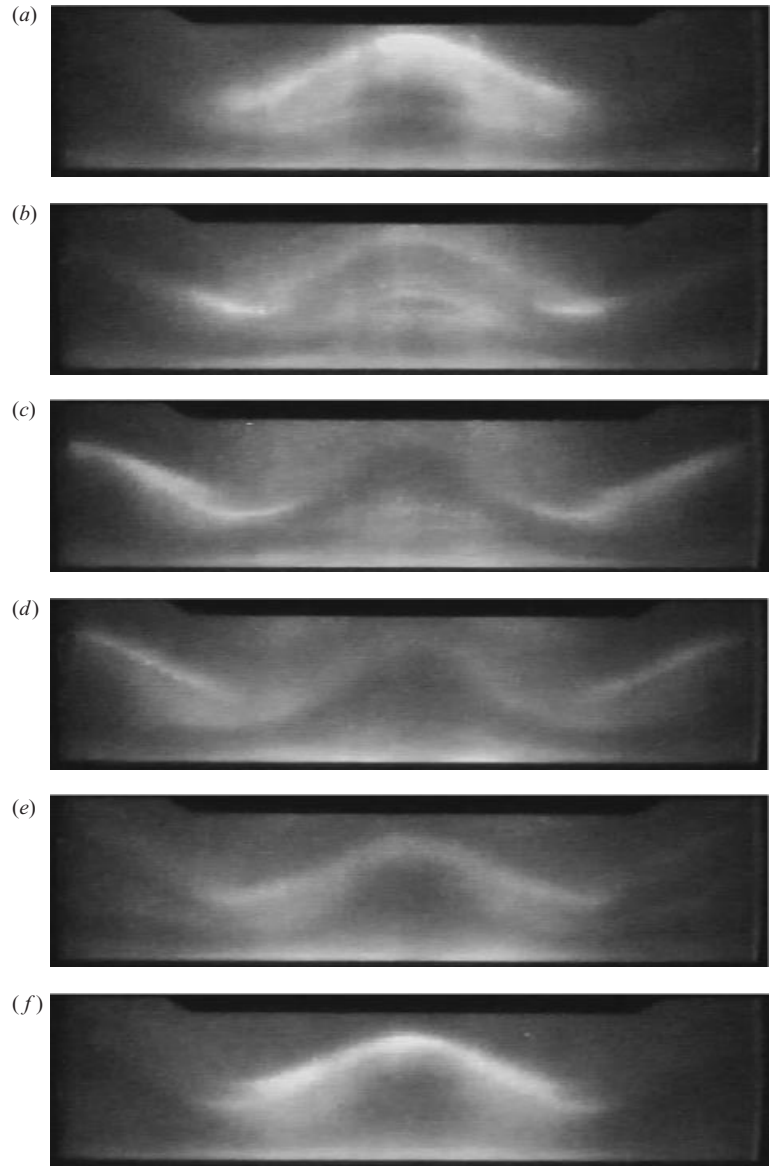

FIGURE 16. Secondary instability mode. Six successive pictures of the flow for the following experimental parameters: $n = 2$, $Re = 2100$ and $H/R = 7.80$. The first picture is taken after 3 min, i.e. $\Omega t = 514$. The time interval between two pictures is $\Omega \Delta t = 0.54$ such that the six pictures represent a full period of the dynamics.

$m_1 = 2$, $\omega_1 = 2.27\Omega$ and $k_2 = \frac{3}{2}k_0$, $m_2 = 3$, $\omega_2 = 2.27\Omega$, with $k_0 = 1.579$ the axial wavenumber of the mode $(-1, 1, 1)$. Mason & Kerswell (1999) predict the presence of a secondary instability mode of frequency $\omega = 2.27\Omega$ as soon as $a > 0.014$ (this number is different from that found in their paper because of different normalizations of the Kelvin modes). In our measurements, the oscillation of the amplitude A after saturation was only observed for $Re > 1000$ which corresponds to $a_{sat} > 0.05$. This apparent discrepancy may be due to the fact that the amplitude of the secondary instability has to be sufficiently large to be observed experimentally. For $Re < 4000$,

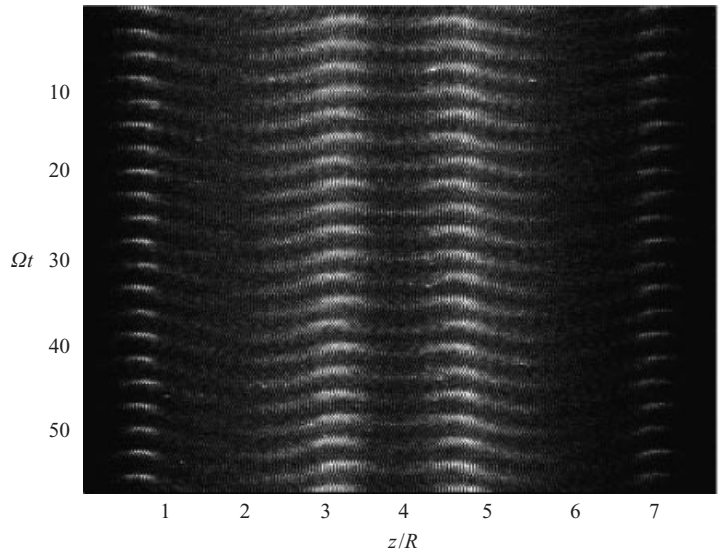

FIGURE 17. Spatio-temporal diagram of the secondary instability mode. This diagram is constructed by extracting a horizontal video line in the top quarter of the cylinder (as seen in figure 16). The experimental parameters are identical to those indicated in figure 16. The signal is time-periodic with a frequency $\omega_{exp} = 2.31\Omega$.

we always observed the saturation of the primary mode and its secondary instability (when present). However, for higher Reynolds numbers, the flow exhibits a new behaviour, as described in the next section.

4.3. *High-Reynolds-number flow*

For $Re > 4000$, the weakly nonlinear theory, as exposed in the previous section, is not sufficient to describe what can be seen by Kalliroscope visualizations. For time-periodic modes of the elliptic instability (all modes different from $(-1, 1, 1)$), or for modes of the triangular instability (all time-periodic), no saturation of the mode amplitude has been observed. Figure 18 shows three successive pictures of the flow for the mode $(-1, 2, 1)$ of the triangular instability. For $Re = 4700$, 4.5 wavelengths of the mode $(-1, 2, 1)$ are first observed along the length of the cylinder (figure 18*a*). This oscillation grows (figure 18*b*) until it eventually leads after a few periods of rotation to an apparent disordered flow (figure 18*c*) which is maintained forever. Unfortunately, because of the short time scale of the phenomenon affecting these periodic modes, it is difficult to carry out PIV measurements and the visualization gives only a qualitative picture of the flow. The apparent small-scale disorder could be the result of the superposition of several modes of the multipolar instability and secondary instability modes. In the literature, this apparent disorder has been called 'resonant collapse' (McEwan 1971), 'wave collapse' (Malkus 1989), 'breakdown' (Kerswell 1999) or 'explosion' (Eloy *et al.* 2000). In the following, we shall use these terms indifferently even if we believe that this state could be explained by a weakly nonlinear interaction of modes as is argued below.

For the stationary mode $(-1, 1, 1)$ of the elliptic instability, the evolution of the flow appears to be different. As mentioned in Eloy *et al.* (2000), there is no saturation of the mode amplitude for such high-Reynolds-number flows. A cycle of instability, explosion and relaminarization can be observed with Kalliroscope visualization (figure 5 of

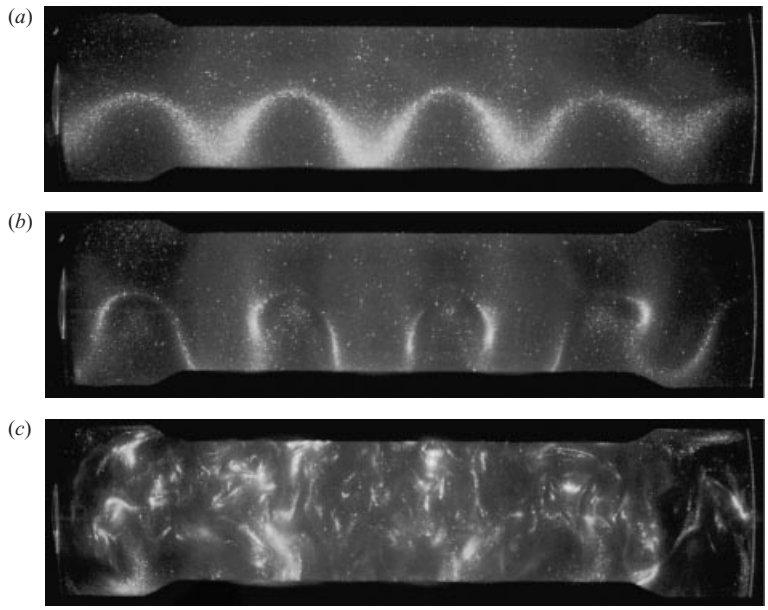

FIGURE 18. Three successive pictures of the flow [mode $(-1, 2, 1)$] for $n = 3$, $Re = 4700$ $H/R = 8$ and (a) $\Omega t = 330$; (b) $\Omega t = 350$; (c) $\Omega t = 420$.

Eloy *et al.* 2000). The first two stages are comparable to what has been observed for time-periodic modes; the instability grows until the flow becomes very disordered (apparently), similar to what can be seen in figure 18 for the mode $(-1, 2, 1)$. This disorder which is characterized by the apparition of small scales appears suddenly (on a time scale comparable to the rotation period) and gives the impression of an 'explosion' of the flow. However, in contrast to time-periodic modes, these 'small scales' are not maintained and the flow eventually relaminarizes to a solid-body rotation. At this stage, the instability can grow again, leading to a characteristic intermittent cycle.

Figure 14 shows how the mode amplitude and phase vary as measured with PIV for $Re = 4700$. It can be seen that the amplitude first grows exponentially until $\Omega t = 250$. At this moment, the amplitude seems to saturate ($a \approx 0.7$) as does its phase ($\varphi \approx 35°$). But when $\Omega t = 300$, the 'explosion' occurs and the amplitude decreases until $\Omega t = 370$. During this decay, the phase varies rapidly giving the impression that the amplitude is spiralling back to zero. Then, from $\Omega t = 400$ to 500, the unstable mode $(-1, 1, 1)$ grows again until the second explosion. The PIV recording ends when the flow has relaminarized for the second time at $\Omega t = 600$. During the whole cycle, the velocity field as measured by PIV is a rotation around a single point (except for very rare velocity fields at the end of the amplitude decay for which there seem to be two rotation centres close to each other). Moreover, the impression of 'small scales' given by the Kalliroscope visualizations is not recovered by PIV measurements. This means that during the cycle, the flow is mainly composed of the mode $(-1, 1, 1)$.

Several scenarios have been proposed in the past to explain the violent explosion observed on visualizations. In the context of forced Kelvin modes, McEwan (1971) first proposed that this 'resonant collapse' (as he named it) could be triggered by the triadic interactions of three Kelvin waves. In the context of precessing instabilities, Kobine (1995) and Manasseh (1996) observed a similar 'collapse'. It has been argued

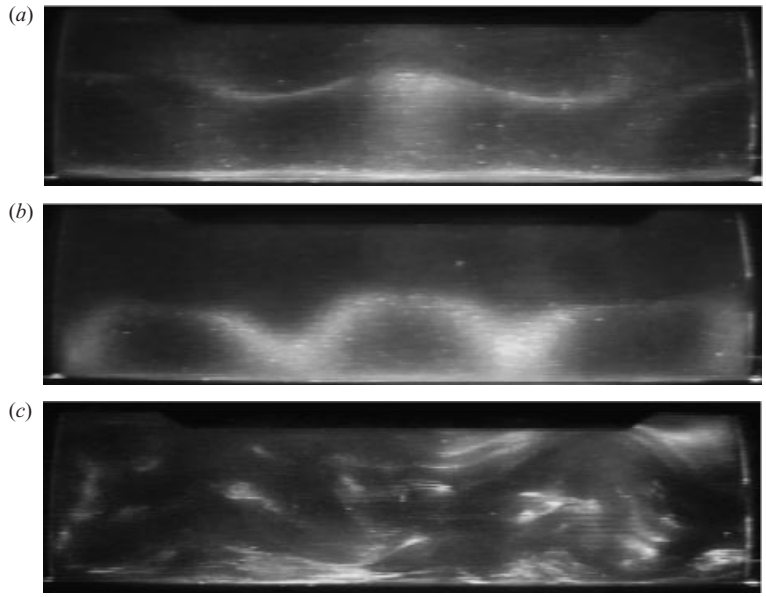

FIGURE 19. Three successive pictures of the flow for $Re = 6600$, $H/R = 8$ and (a) $\Omega t = 61$; (b) $\Omega t = 63$; (c) $\Omega t = 80$.

that boundary-layer instabilities or a centrifugal instability could be responsible for this collapse. Malkus & Waleffe (1991) proposed a third scenario. They claimed that, owing to nonlinear interactions, the basic flow enters a regime (defined by $\mathrm{d}\Gamma^2/\mathrm{d}r < \Gamma^2/r$ where $\Gamma(r)$ is the circulation) where Kelvin modes no longer exist. They attributed the 'collapse' to this regime. Finally, Mason & Kerswell (1999) and Kerswell (2002) argued that the secondary instability could be the first step of a bifurcation cascade (in the spirit of Ruelle–Takens) leading to the violent collapse. Despite the number of scenarios, no clear experimental fact has so far been able to clarify the mechanism of 'explosion'.

In our experiment, we have tried to test the different scenarios. We first analysed the velocity field given by PIV measurements. It appeared that the Rayleigh criterion for centrifugal instability and the criterion on the circulation $\Gamma(r)$ proposed by Malkus & Waleffe (1991) were never satisfied throughout the whole cycle of instability and explosion. These two scenarios can therefore be discarded. As explained in the previous section, for sufficiently small Reynolds number ($Re < 4000$), the secondary instability described by Kerswell (1999) has been shown experimentally. However, it was also shown that the presence of this secondary instability does not lead to explosion in this regime. For larger Reynolds numbers, this secondary instability is probably also present even if it is difficult to visualize experimentally because of the short duration of the explosion. On particular visualizations such as those in figure 19, just prior to explosion, two different modes of the primary elliptic instability have been observed. In figure 19(a), we can see the two wavelengths characterizing the mode $(-1, 1, 1)$ and, a short time later (less than half the rotation period), a mode with 3 wavelengths in figure 19(b). A spatio-temporal diagram (not shown here) permits us to measure the period of the flow: $\omega = 1.0\Omega$, and therefore confirms that the second mode observed is the primary mode $(0, 2, 1)$. This means that these two modes can coexist before explosion. Their interaction could thus play a role in the collapse observed later. Note, however, that this superposition of the mode $(-1, 1, 1)$

and $(0, 2, 1)$ is not always observed in Kalliroscope visualizations and that it was not observed in PIV measurements.

Based on these experimental facts, we can argue that the mechanism of 'collapse' is likely to be a nonlinear interaction of several modes of the primary or secondary instability. However, it is difficult to distinguish which mode interacts with the mode $(-1, 1, 1)$ since both the secondary instability mode and the mode $(0, 2, 1)$ involve a Kelvin mode of azimuthal wavenumber $m = 2$ and with a wavelength λ such that $3\lambda = H/R$. As Mason & Kerswell (1999) observed numerically, the secondary instability could force the mode $(0, 2, 1)$. This may explain why it can be visible on few visualizations. Besides, any defect of the experiment (such as a non-homogeneous cylinder material) may drive a forcing at the rotation frequency Ω which is precisely the frequency of the mode $(0, 2, 1)$. We can imagine that the mode $(0, 2, 1)$ created this way could also force the secondary instability mode. In any case, the presence of another mode modifies the weakly nonlinear amplitude equations obtained in the previous section. Indeed, the equation for the geostrophic modes would have to take into account the presence of these additional modes. This could be sufficient to completely change the dynamics of the $(-1, 1, 1)$ mode amplitude and generate the cycle of instability–explosion observed.

5. Conclusion

In this paper, we have studied experimentally and theoretically the stability of a vortex subjected to a dipolar or tripolar stationary strain. The experimental apparatus is made of an elastic deformable cylinder rotated at constant angular speed. This cylinder is constrained by two or three rollers to deform it elliptically or triangularly. We have studied the flow under the variation of two dimensionless control parameters: the aspect ratio of the cylinder which can be varied by changing its length and the Reynolds number based on the angular speed. The third control parameter could be the strength of the applied constraint, but its variation has not been studied in the present paper. We have shown theoretically by studying the viscous linear stability of the flow that these two control parameters are able to select particular modes of the instability. A diagram showing the most unstable mode as a function of the Reynolds number and aspect ratio has been constructed (figure 9). This predicted diagram shows excellent agreement with the experimentally observed modes close to the instability threshold. In particular, we have exhibited time-periodic modes which were not reported by previous experimental studies.

The instability has also been studied for Reynolds numbers far from the threshold for the stationary undulating modes. For the first time, we have demonstrated that a viscous weakly nonlinear analysis is able to predict the dynamics of the mode amplitude as measured by PIV up to $Re = 4000$. The weakly nonlinear interaction of the mode with itself drives a geostrophic mode whose effect is to modify the basic flow. The growth of the geostrophic mode forces a detuning of the mode phase which yields a stabilizing effect. In all cases, the weakly nonlinear equations lead to stable fixed points with saturated amplitude. The amplitude of the predicted fixed points depends on the Reynolds number, it compares well with the PIV measurement of the saturated mode amplitude. Through Kalliroscope visualizations, we have also shown the presence of a secondary instability as predicted by Kerswell (1999) in his numerical study. The secondary instability mode amplitude has been shown to saturate experimentally for $Re < 4000$. However, for

higher Reynolds number, the flow exhibits a new behaviour. After the growth of the unstable mode, an 'explosion' of the flow has been observed. This 'collapse' is probably due to the growth of a geostrophic mode driven by the nonlinear interaction of secondary instability modes or other modes of the primary instability. This geostrophic mode modifies the mean flow and therefore changes the dynamics of the mode amplitude giving the impression of a violent 'explosion'. In other words, this apparent 'collapse' could be nothing but a complex weakly nonlinear interaction of the fundamental modes with secondary instability modes and the geostrophic flow.

In this paper, we have investigated the multipolar instability which is a resonant vortex instability. Its physical mechanism lies in the interaction of two natural Kelvin modes of the vortex with the applied constraint. In the case studied here, the constraint can be viewed as a two-dimensional stationary intrinsic 'mode', i.e. with axial wavenumber, azimuthal wavenumbers and frequency $k = 0$, $m = n$ and $\omega = 0$. In the context of turbulent flows, it would be interesting to study the effect of any general intrinsic mode $[k; m; \omega]$. Indeed, combinations of such general modes would give a model of the turbulent field surrounding vortex filaments. Such a constraint is likely to drive a resonant instability similar to the multipolar instability. The richness of this kind of resonant instability could explain the splitting and undulation of vortex filaments seen in turbulent flows both experimentally (Cadot *et al.* 1995) and numerically (Arendt *et al.* 1998).

We would like to acknowledge the valuable help of Patrice Meunier during the experimental study.

Appendix. Mathematical expressions

A.1. *Kelvin modes*

The velocity–pressure field of a Kelvin mode is defined by (3.2) where $\boldsymbol{U} = (-\mathrm{i}U_r; U_\theta; U_z; P)$ is given by:

$$U_r(r) = (m-\omega)\delta J'_{|m|}(\delta r) + \frac{2m}{r} J_{|m|}(\delta r), \tag{A 1a}$$

$$U_\theta(r) = 2\delta J'_{|m|}(\delta r) + \frac{m(m-\omega)}{r} J_{|m|}(\delta r), \tag{A 1b}$$

$$U_z(r) = -\frac{k}{m-\omega}[4-(m-\omega)^2] J_{|m|}(\delta r), \tag{A 1c}$$

$$P(r) = [4-(m-\omega)^2] J_{|m|}(\delta r), \tag{A 1d}$$

where J_μ is the Bessel function of the first kind and J'_μ its derivative. The scalar δ in these expressions is the 'radial wavenumber' and is defined as:

$$\delta^2 = \frac{k^2(2+m-\omega)(2-m+\omega)}{(m-\omega)^2}. \tag{A 2}$$

The dispersion relation $D(k, m, \omega) = 0$ is given by

$$D(k, m, \omega) = (m-\omega)\delta J'_{|m|}(\delta) + 2m J_{|m|}(\delta). \tag{A 3}$$

A.2. *Operators*

The operators required to calculate amplitude equations (3.4*a*), and (3.4*b*) are:

$$\mathscr{I} = \begin{pmatrix} 1 & 0 & 0 & 0 \\ 0 & 1 & 0 & 0 \\ 0 & 0 & 1 & 0 \\ 0 & 0 & 0 & 0 \end{pmatrix}, \tag{A 4}$$

$$\mathscr{Q} = \begin{pmatrix} 0 & 0 & 0 & 0 \\ 0 & 0 & 0 & 0 \\ 0 & 0 & 0 & 1 \\ 0 & 0 & 1 & 0 \end{pmatrix}, \tag{A 5}$$

$$\mathscr{N} = \frac{1}{2}\begin{pmatrix} \mathrm{D}_1 - (n-1)r^{n-2} & -\mathrm{i}(n-2)r^{n-2} & 0 & 0 \\ -\mathrm{i}nr^{n-2} & \mathrm{D}_1 + (n-1)r^{n-2} & 0 & 0 \\ 0 & 0 & \mathrm{D}_1 & 0 \\ 0 & 0 & 0 & 0 \end{pmatrix}, \tag{A 6}$$

with

$$\mathrm{D}_1 = -r^{n-1}\frac{\partial}{\partial r} + mr^{n-2}, \tag{A 7}$$

$$\mathscr{L} = \begin{pmatrix} \mathrm{D}_2 - \dfrac{1}{r^2} & -\dfrac{2\mathrm{i}m}{r^2} & 0 & 0 \\ \dfrac{2\mathrm{i}m}{r^2} & \mathrm{D}_2 - \dfrac{1}{r^2} & 0 & 0 \\ 0 & 0 & \mathrm{D}_2 & 0 \\ 0 & 0 & 0 & 0 \end{pmatrix}, \tag{A 8}$$

and

$$\mathrm{D}_2 = \frac{1}{r}\frac{\partial}{\partial r} + \frac{\partial^2}{\partial r^2} - \frac{m^2}{r^2} + \frac{\partial^2}{\partial z^2}. \tag{A 9}$$

A.3. *Linear amplitude equations*

As in Moore & Saffman (1975) and Eloy & Le Dizès (2001), linear amplitude equations are obtained from solvability conditions. Explicit and compact expressions for the linear coefficients can be obtained if we introduce the scalar product:

$$\langle \boldsymbol{X} | \boldsymbol{Y} \rangle = \int_0^1 (\overline{X}_r Y_r + \overline{X}_\theta Y_\theta + \overline{X}_z Y_z + \overline{X}_p Y_p) r \, \mathrm{d}r, \tag{A 10}$$

and the notation:

$$\mathscr{N}_{2|1} = \langle \boldsymbol{U}^{(2)} | \mathscr{N} \boldsymbol{U}^{(1)} \rangle, \tag{A 11}$$

where $\boldsymbol{U}^{(1)}$ and $\boldsymbol{U}^{(2)}$ are the velocity–pressure fields of the first and second Kelvin modes, respectively. Using similar techniques to those in Eloy & Le Dizès (2001), we obtain for the coefficients appearing in (3.4*a*) and (3.4*b*)

$$n_1 = \frac{\overline{\mathscr{N}}_{1|2} - I_1}{\mathscr{I}_{1|1}}, \quad v_1 = -\frac{\mathscr{L}_{1|1}}{\mathscr{I}_{1|1}}, \quad q_1 = \frac{\mathscr{Q}_{1|1}}{\mathscr{I}_{1|1}}, \tag{A 12a–c}$$

$$n_2 = \frac{\mathscr{N}_{2|1} - I_2}{\mathscr{J}_{2|2}}, \quad v_2 = -\frac{\mathscr{L}_{2|2}}{\mathscr{J}_{2|2}}, \quad q_2 = \frac{\mathscr{Q}_{2|2}}{\mathscr{J}_{2|2}}, \tag{A 12d–f}$$

where the bar denotes complex conjugation, the terms I_1 and I_2 originate from the inviscid elliptic boundary conditions and are evaluated in $r = 1$:

$$I_1 = \tfrac{1}{2}P^{(1)}\left(U_\theta^{(2)} + \frac{1}{n}\frac{\partial U_r^{(2)}}{\partial r}\right), \tag{A 13a}$$

$$I_2 = \tfrac{1}{2}P^{(2)}\left(U_\theta^{(1)} - \frac{1}{n}\frac{\partial U_r^{(1)}}{\partial r}\right). \tag{A 13b}$$

The terms s_1 and s_2 come from the viscous boundary conditions. Kudlick (1966) gave explicit expressions:

$$s_1 = \frac{(4-\zeta_1^2)}{4\sqrt{2}(m_1^2 + k^2 + \frac{1}{2}m_1\zeta_1)}\frac{R}{H}\left[(1-\mathrm{i})\frac{2-\zeta_1}{\sqrt{2+\zeta_1}}\left(m_1^2 + k^2 + \frac{2m_1\zeta_1}{2-\zeta_1}\right)\right. \tag{A 14a}$$

$$\left. + (1+\mathrm{i})\frac{2+\zeta_1}{\sqrt{2-\zeta_1}}\left(m_1^2 + k^2 + \frac{2m_1\zeta_1}{2+\zeta_1}\right) + (1-\mathrm{i})\left(m_1^2 + k^2\right)\frac{H}{R}\sqrt{\zeta_1}\right], \tag{A 14b}$$

$$s_2 = \frac{(4-\zeta_2^2)}{4\sqrt{2}(m_2^2 + k^2 - \frac{1}{2}m_2\zeta_2)}\frac{R}{H}\left[(1+\mathrm{i})\frac{2-\zeta_2}{\sqrt{2+\zeta_2}}\left(m_2^2 + k^2 - \frac{2m_2\zeta_2}{2-\zeta_2}\right)\right. \tag{A 14c}$$

$$\left. + (1-\mathrm{i})\frac{2+\zeta_2}{\sqrt{2-\zeta_2}}\left(m_2^2 + k^2 - \frac{2m_2\zeta_2}{2+\zeta_2}\right) + (1+\mathrm{i})\left(m_2^2 + k^2\right)\frac{H}{R}\sqrt{\zeta_2}\right], \tag{A 14d}$$

with

$$\zeta_1 = |\omega - m_1|, \quad \zeta_2 = |\omega - m_2|. \tag{A 15a, b}$$

REFERENCES

Aldridge, K., Seyed-Mahmoud, B., Henderson, G. & van Wijngaarden, W. 1997 Elliptical instability of the Earth's fluid core. *Phys. Earth Planet. Int.* **103**, 365–374.

Arendt, S., Fritts, D. C. & Andreassen, Ø. 1998 Kelvin twist waves in the transition to turbulence. *Eur. J. Mech.* B/*Fluids* **17**, 595–604.

Bayly, B. J. 1986 Three-dimensional instability of elliptical flow. *Phys. Rev. Lett.* **57**, 2160–2163.

Bayly, B. J., Holm, D. D. & Lifschitz, A. 1996 Three-dimensional stability of elliptical vortex columns in external strain flows. *Phil. Trans. R. Soc. Lond.* A **354**, 895–926.

Bayly, B. J., Orszag, S. A. & Herbert, T. 1988 Instability mechanisms in shear-flow transition. *Annu. Rev. Fluid Mech.* **20**, 359–391.

Billant, P., Brancher, P. & Chomaz, J.-M. 1999 Three dimensional stability of a vortex pair. *Phys. Fluids* **11**, 2069–2077.

Burgers, J. M. 1948 A mathematical model illustrating the theory of turbulence. *Adv. Appl. Mech.* **1**, 171–199.

Cadot, O., Douady, S. & Couder, Y. 1995 Characterization of the low pressure filaments in three-dimensional turbulent shear flow. *Phys. Fluids* **7**, 630–646.

Chernous'ko, Y. L. 1978 An experimental study of secondary multi-eddy flows in elliptical cylinders. *Izv. Akad. Nauk SSSR FAO* **14**, 151–153.

Eloy, C. & Le Dizès, S. 1999 Three-dimensional instability of Burgers and Lamb–Oseen vortices in a strain field. *J. Fluid Mech.* **378**, 145–166.

Eloy, C. & Le Dizès, S. 2001 Stability of the Rankine vortex in a multipolar strain field. *Phys. Fluids* **13**, 660–676.

Eloy, C., Le Gal, P. & Le Dizès, S. 2000 Experimental study of the multipolar vortex instability. *Phys. Rev. Lett.* **85**, 3400–3403.

Fabijonas, B., Holm, D. D. & Lifschitz, A. 1997 Secondary instabilities of flows with elliptical streamlines. *Phys. Rev. Lett.* **78**, 1900–1903.

Gauthier, G., Gondret, P. & Rabaud, M. 1998 Motions of anisotropic particules: application to visualization of three-dimensional flows. *Phys. Fluids* **10**, 2147–2154.

Gledzer, E. B., Dolzhanskiy, F. V., Obukhov, A. M. & Ponomarev, V. M. 1975 An experimental and theoretical study of the stability of motion of a liquid in an elliptical cylinder. *Izv. Acad. Sci. USSR Atmos. Oceanic Phys.* **11**, 617–622.

Gledzer, E. B., Novikov, Y. V., Obukhov, A. M. & Chusov, M. A. 1974 An investigation of the stability of liquid flows in a three-axis ellipsoid. *Izv. Acad. Sci. USSR Atmos. Oceanic Phys.* **10**, 69–71.

Gledzer, E. B. & Ponomarev, V. M. 1992 Instability of bounded flows with elliptical streamlines. *J. Fluid Mech.* **240**, 1–30.

Greenspan, H. P. 1968 *The Theory of Rotating Fluids*. Cambridge University Press.

Jiménez, J. & Wray, A. A. 1998 On the characteristics of vortex filaments in isotropic turbulence. *J. Fluid Mech.* **373**, 255–285.

Kelvin, Lord 1880 Vibrations of a columnar vortex. *Phil. Mag.* **10**, 155–168.

Kerswell, R. R. 1994 Tidal excitation of hydromagnetic waves and their damping in the earth. *J. Fluid Mech.* **274**, 219–241.

Kerswell, R. R. 1999 Secondary instabilities in rapidly rotating fluids: inertial wave breakdown. *J. Fluid Mech.* **382**, 283–306.

Kerswell, R. R. 2002 Elliptical instability. *Annu. Rev. Fluid Mech.* **34**, 83–113.

Kerswell, R. R. & Barenghi, C. F. 1995 On the viscous decay rates of inertial waves in a rotating cylinder. *J. Fluid Mech.* **285**, 203–214.

Kerswell, R. R. & Malkus, W. V. R. 1998 Tidal instability as the source for Io's magnetic signature. *Geophys. Res. Lett.* **25**, 603–606.

Kida, S. & Ohkitani, K. 1992 Spatiotemporal intermittency and instability of a forced turbulence. *Phys. Fluids* A **4**, 1018–1027.

Kobine, J. J. 1995 Inertial wave dynamics in a rotating and precessing cylinder. *J. Fluid Mech.* **303**, 233–252.

Kudlick, M. 1966 On the transient motions in a contained rotating fluid. PhD thesis, Massachussets Institute of Technology.

Le Dizès, S. & Eloy, C. 1999 Short-wavelength instability of a vortex in a multipolar strain field. *Phys. Fluids* **11**, 500–502.

Leweke, T. & Williamson, C. H. K. 1998*a* Cooperative elliptic instability of a vortex pair. *J. Fluid Mech.* **360**, 85–119.

Leweke, T. & Williamson, C. H. K. 1998*b* Three-dimensional instabilities in wake transition. *Eur. J. Mech.* B/*Fluids* **17**, 571–586.

Lifschitz, A. & Fabijonas, B. 1996 A new class of instabilities of rotating fluids. *Phys. Fluids* **8**, 2239–2241.

McEwan, A. D. 1971 Degeneration of resonantly-excited standing internal gravity waves. *J. Fluid Mech.* **50**, 431–448.

Malkus, W. V. R. 1989 An experimental study of global instabilities due to tidal (elliptical) distortion of a rotating elastic cylinder. *Geophys. Astrophys. Fluid Dyn.* **48**, 123–134.

Malkus, W. V. R. & Waleffe, F. A. 1991 Transition from order to disorder in elliptical flow: a direct path to shear flow turbulence. In *Advances in turbulence III* (ed. A. V. Johansson & P. H. Alfredsson). Springer.

Manasseh, R. 1996 Nonlinear behaviour of contained inertia waves. *J. Fluid Mech.* **315**, 151–173.

Mason, D. M. & Kerswell, R. R. 1999 Nonlinear evolution of the elliptical instability: an example of inertial breakdown. *J. Fluid Mech.* **396**, 73–108.

Meunier, P. & Leweke, T. 2001 Three-dimensional instability during vortex merging. *Phys. Fluids* **13**, 2747–2750.

Meunier, P. & Leweke, T. 2002 Analysis and minimization of errors due to high gradients in particle image velocimetry. *Exps. Fluids* (submitted).

Moffatt, H. K., Kida, S. & Ohkitani, K. 1994 Stretched vortices – the sinews of turbulence; large-Reynolds-number asymptotics. *J. Fluid Mech.* **259**, 241–264.

Moore, D. W. & Saffman, P. G. 1975 The instability of a straight vortex filament in a strain field. *Proc. R. Soc. Lond.* A **346**, 413–425.

Passot, T., Politano, H., Sulem, P.-L., Angilella, J. R. & Meneguzzi, M. 1995 Instability of strained vortex layers and vortex tube formation in homogeneous turbulence. *J. Fluid Mech.* **282**, 313–338.

Pierrehumbert, R. T. 1986 Universal short-wave instability of two-dimensional eddies in an inviscid fluid. *Phys. Rev. Lett.* **57**, 2157–2160.

Prochazka, A. & Pullin, D. I. 1998 Structure and stability of non-symmetric Burgers vortices. *J. Fluid Mech.* **363**, 199–228.

Pullin, D. I. & Saffman, P. G. 1998 Vortex dynamics in turbulence. *Annu. Rev. Fluid Mech.* **30**, 31–51.

Racz, J.-P. & Scott, J. F. 2001*a* Instability in a rotating cylinder with sinusoidal compression. Part 1. Linear theory. *J. Fluid Mech.* (submitted).

Racz, J.-P. & Scott, J. F. 2001*b* Instability in a rotating cylinder with sinusoidal compression. Part 2. Weakly nonlinear theory. *J. Fluid Mech.* (submitted).

Rieutord, M. & Valdetarro, L. 1997 Inertial waves in a rotating spherical shell. *J. Fluid Mech.* **341**, 77–99.

Seyed-Mahmoud, B., Henderson, G. & Aldridge, K. 2000 A numerical model for elliptical instability of the Earth's fluid outer core. *Phys. Earth Planet. Int.* **117**, 51–61.

Sipp, D. 2000 Weakly nonlinear saturation of short-wave instabilities in a strained Lamb–Oseen vortex. *Phys. Fluids* **12**, 1715–1729.

Ting, L. & Tung, C. 1965 Motion and decay of a vortex in a nonuniform stream. *Phys. Fluids* **8**, 1039–1051.

Tsai, C.-Y. & Widnall, S. E. 1976 The stability of short waves on a straight vortex filament in a weak externally imposed strain field. *J. Fluid Mech.* **73**, 721–733.

Waleffe, F. 1989 The 3D instability of a strained vortex and its relation to turbulence. PhD thesis, Massachusetts Institute of Technology.

Watkins, W. B. & Hussey, R. G. 1977 Spin-up from rest in a cylinder. *Phys. Fluids* **20**, 1596–1604.

Wedemeyer, E. H. 1964 The unsteady flow within a spinning cylinder. *J. Fluid Mech.* **20**, 383–399.